Self-organized structures of two-component laser fields and their active control in a cold Rydberg atomic gas

Zeyun Shi[1] and Guoxiang Huang[1,2,3]

[1]*State Key Laboratory of Precision Spectroscopy, East China Normal University, Shanghai 200062, China*

[2]*NYU-ECNU Joint Institute of Physics, New York University Shanghai, Shanghai 200062, China*

[3]*Collaborative Innovation Center of Extreme Optics, Shanxi University, Taiyuan, Shanxi 030006, China*

(Received 3 January 2021; accepted 28 June 2021; published 12 July 2021)

We investigate the formation and control of stationary optical patterns in a cold Rydberg atomic gas via double electromagnetically induced transparency. We show that, through the modulational instability of the plane-wave state of a laser field with two polarization components, the system undergoes a spontaneous symmetry breaking and hence the emergence of plentiful self-organized spatial optical structures, which can be manipulated by the ratio between the cross- and self-Kerr nonlinearities, the nonlocality degree of the Kerr nonlinearities, and the populations initially prepared in the two atomic ground states. Interestingly, a crossover from mixture to separation in space (optical phase separation) of the two polarization components occurs when the ratio between the cross- and self-Kerr nonlinearities exceeds a critical value. We also show that the system supports nonlocal two-component spatial optical solitons and vortices when the parameters of the system are selected suitably. The rich diversity and active controllability of the self-organized optical structures reported here provide a way for realizing novel optical patterns and solitons and their structural phase transitions based on Rydberg atomic gases.

DOI: 10.1103/PhysRevA.104.013511

I. INTRODUCTION

In the past two decades, much attention has been paid to the study of cold Rydberg atomic gases [1,2] working under condition of electromagnetically induced transparency (EIT) [3,4]. EIT is an important quantum interference effect typically occurring in resonant three-level atomic systems, by which the absorption of a probe laser field can be greatly suppressed by a control laser field [5]. Due to the strong interaction between Rydberg atoms (also called Rydberg-Rydberg interaction), Rydberg gases are ideal nonlinear optical media to acquire giant enhancement of optical Kerr nonlinearity if the Rydberg-Rydberg interaction is mapped to photon-photon interaction via EIT [6,7].

In addition to the giant enhancement, the Kerr nonlinearity in Rydberg gases possesses many other interesting properties. One of them is its nonlocality, originated from the long-range character of the Rydberg-Rydberg interaction [8–15]. Based on such nonlocality, Sevincli *et al.* [8] showed that a hexagonal optical pattern can spontaneously form through a modulational instability (MI) of a plane-wave probe field in a ladder-shaped three-level Rydberg gas (Rydberg-EIT) with repulsive Rydberg-Rydberg interaction. Recently, it was demonstrated that a structural phase transition of optical patterns from a hexagonal lattice to two types of square lattices may occur in an EIT-based Rydberg gas with a microwave dressing between two Rydberg states [16]. These investigations enriched our understanding of the MI and related pattern formation in systems with repulsive (or with both repulsive and attractive) Kerr nonlinearities, which are topics explored in different physical systems by many research groups, from which new pattern formation mechanisms for conservative nonlocal nonlinear systems were found in recent years [17–36].

In this paper, we consider the formation and manipulation of stationary optical patterns in a cold four-state Rydberg gas with a repulsive Rydberg-Rydberg interaction. The atoms under study have an inverted Y-shaped level configuration, interacting with a control field and a probe field with two orthogonal polarization components and working under the condition of double Rydberg-EIT [37]. Starting from Maxwell-Bloch (MB) equations and using an approach on atom-atom correlations beyond the mean-field approximation, we derive two coupled three-dimensional (3D) nonlocal nonlinear Schrödinger (NNLS) equations, in which nonlocal self- and cross-Kerr nonlinearities display specific characters. Based on the MI analysis of the plane-wave state of the probe field, we show that the system can undergo a spontaneous symmetry breaking, resulting in the emergence of novel self-organized optical structures.

Through detailed analytical and numerical calculations, we find that the plane-wave state can be transited into many (at least eight) types of self-organized spatial optical lattice patterns. These optical patterns are controlled by the ratio between the cross- and self-Kerr nonlinearities, the nonlocality degree of the Kerr nonlinearities, and the populations initially prepared in the two atomic ground states. Interestingly, a crossover from spatial mixture to spatial separation (i.e., optical phase separation) for the two polarization components of the probe field may appear when the ratio between the cross- and self-Kerr nonlinearities reaches beyond a critical value. We also show that the system can support nonlocal two-component spatial optical solitons and vortices if the

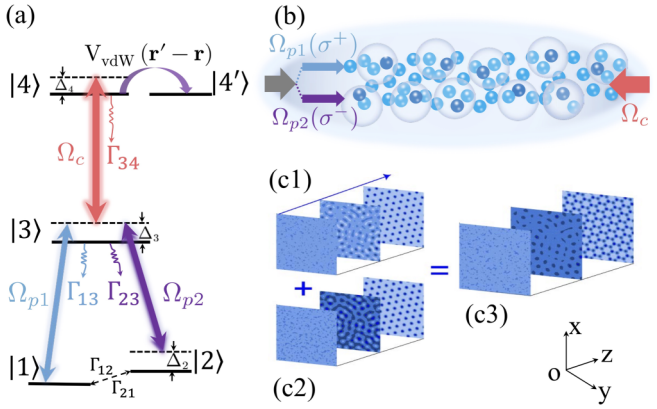

FIG. 1. (a) Atomic level diagram and inverted Y-shaped excitation scheme supporting the double Rydberg-EIT. The σ^+ (σ^-) polarization component of the probe field [half Rabi frequency Ω_{p1} (Ω_{p2})] drives the transition $|1\rangle \leftrightarrow |3\rangle$ ($|2\rangle \leftrightarrow |3\rangle$)); the strong control field with half Rabi frequency Ω_c drives the transition $|3\rangle \leftrightarrow |4\rangle$. $|1\rangle$ and $|2\rangle$: ground states; $|3\rangle$: intermediate excited state; $|4\rangle$: highly excited Rydberg state; Δ_3: one-photon detunings; Δ_2 and Δ_4: two-photon detunings; Γ_{13}, Γ_{23}, and Γ_{34}: spontaneous emission decay rates; Γ_{12} and Γ_{21}: rates of incoherent population transfer between the two ground states; $V_{\rm vdW}(\mathbf{r}'-\mathbf{r}) \equiv \hbar\mathcal{V}(\mathbf{r}'-\mathbf{r})$: the van der Waals potential describing the interaction between two Rydberg atoms located, respectively, at positions $\mathbf{r}$ and $\mathbf{r}'$. (b) Possible experimental geometry, where small solid circles denote atoms, and large transparent spheres denote Rydberg blockade spheres in which only one atom is excited into a Rydberg state. (c1)–(c3) Pattern formation via the modulation instability of a plane-wave probe field, where (c1) [(c2)] represents the σ^+ (σ^-) polarization component, and (c3) represents their superposition (total probe field).

parameters of the system are selected suitably to make the signs of the Kerr nonlinearities change. The rich diversity in the types and active controllability in the properties of the self-organized optical structures found in this work provide ways for realizing novel optical patterns and solitons and for manipulating their structural phase transitions by exploiting Rydberg gases via EIT.

The remainder of the paper is arranged as follows. In Sec. II, we present the physical model of the double Rydberg-EIT under study, and we derive two coupled 3D NNLS equations describing the evolution of the two polarized components of the probe field beyond the mean-field approximation. In Sec. III, we consider the MI of a plane-wave state, and we investigate the pattern formation, structural phase transition, optical phase separation, and nonlocal optical soliton and vortices in the system. Finally, Sec. IV gives a summary of the main results obtained in our work.

II. MODEL AND COUPLED NONLINEAR ENVELOPE EQUATIONS

A. Physical model

We start to consider an ensemble of lifetime-broadened four-level atoms with an inverted Y-shaped excitation scheme [see Fig. 1(a)]. Here the σ^+ (σ^-) polarization component of a weak probe field $\mathbf{E}_p$ [with angular frequency ω_p, wave vector $\mathbf{k}_{p+}$ ($\mathbf{k}_{p-}$), and half Rabi frequency Ω_{p1} (Ω_{p2})] drives the transition $|1\rangle \leftrightarrow |3\rangle$ ($|2\rangle \leftrightarrow |3\rangle$)); the strong, linearly polarized control field with half Rabi frequency Ω_c drives the transition $|3\rangle \leftrightarrow |4\rangle$; $|1\rangle$ and $|2\rangle$ are two ground states, $|3\rangle$ is an intermediate excited state, and $|4\rangle$ is a highly excited Rydberg state; Δ_3 and $\Delta_{2,4}$ are, respectively, one- and two-photon detunings; Γ_{13}, Γ_{23}, and Γ_{34} are spontaneous emission decay rates; Γ_{12} and Γ_{21} are rates of incoherent population transfer between the two ground states.

The total electric field in the system reads $\mathbf{E}(\mathbf{r},t) = \mathbf{E}_p + \mathbf{E}_c = \hat{\mathbf{e}}_+\mathcal{E}_{p+}\exp[i(\mathbf{k}_+\cdot\mathbf{r}-\omega_p t)] + \hat{\mathbf{e}}_-\mathcal{E}_{p-}\exp[i(\mathbf{k}_-\cdot\mathbf{r}-\omega_p t)] + \hat{\mathbf{e}}_c\mathcal{E}_c\exp[i(\mathbf{k}_c\cdot\mathbf{r}-\omega_c t)] + \text{c.c.}$, where $\hat{\mathbf{e}}_\pm = (\hat{\mathbf{e}}_x \pm i\hat{\mathbf{e}}_y)/\sqrt{2}$ and $\mathcal{E}_{p\pm}$ are, respectively, unit polarization vectors and the envelopes of the $\sigma^\pm$-polarization component of the probe field [$\hat{\mathbf{e}}_x$ ($\hat{\mathbf{e}}_y$) is the unit vector along the x (y) direction], and $\hat{\mathbf{e}}_c$ and $\mathcal{E}_c$ are, respectively, the unit polarization vector and amplitude of the control field. Note that the transition paths $|1\rangle \to |3\rangle \to |4\rangle$ and $|2\rangle \to |3\rangle \to |4\rangle$ constitute two ladder-shaped level configurations (each of them displays a Rydberg-EIT), and hence the system supports a double Rydberg-EIT. The interaction between two Rydberg atoms located, respectively, at $\mathbf{r}$ and $\mathbf{r}'$ is described by the van der Waals (vdW) potential $V_{\rm vdW}(\mathbf{r}'-\mathbf{r}) \equiv \hbar\mathcal{V}(\mathbf{r}'-\mathbf{r})$. A possible experimental geometry is presented in Fig. 1(b).

The Hamiltonian of the system is given by $\hat{H} = \mathcal{N}_a\int d^3r\,\hat{\mathcal{H}}_0(\mathbf{r},t) + (\mathcal{N}_a/2)\int d^3r\,\hat{\mathcal{H}}_1(\mathbf{r},t)$. Here $d^3r = dx\,dy\,dz$, $\mathcal{N}_a$ is the atomic density, $\hat{\mathcal{H}}_0(\mathbf{r},t)$ is the Hamiltonian density describing the atoms and the interaction between the atoms and light fields, and $\hat{\mathcal{H}}_1(\mathbf{r},t)$ is the Hamiltonian density describing the Rydberg-Rydberg interaction. Under the electric-dipole and rotating-wave approximations, $\hat{\mathcal{H}}_0$ and $\hat{\mathcal{H}}_1$ have the forms

$$\hat{\mathcal{H}}_0 = -\hbar\sum_{\alpha=2}^{4}\Delta_\alpha\hat{S}_{\alpha\alpha} - \hbar(\Omega_{p1}\hat{S}_{13} + \Omega_{p2}\hat{S}_{23} + \Omega_c\hat{S}_{34} + \text{H.c.}), \tag{1a}$$

$$\hat{\mathcal{H}}_1 = \mathcal{N}_a\int d^3r'\hat{S}_{44}(\mathbf{r},t)\hbar\mathcal{V}(\mathbf{r}'-\mathbf{r})\hat{S}_{44}(\mathbf{r}',t), \tag{1b}$$

where $\hat{S}_{\alpha\beta} = |\beta\rangle\langle\alpha|\exp\{i[(\mathbf{k}_\beta-\mathbf{k}_\alpha)\cdot\mathbf{r} - (\omega_\beta-\omega_\alpha+\Delta_\beta-\Delta_\alpha)t]\}$ is the atomic transition (for $\alpha\neq\beta$) and population (for $\alpha=\beta$) operators, satisfying the commutation relation $[\hat{S}_{\alpha\beta}(\mathbf{r},t),\hat{S}_{\alpha'\beta'}(\mathbf{r}',t)] = \mathcal{N}_a^{-1}\delta(\mathbf{r}-\mathbf{r}')[\delta_{\alpha\beta'}\hat{S}_{\alpha'\beta}(\mathbf{r},t) - \delta_{\alpha'\beta}\hat{S}_{\alpha\beta'}(\mathbf{r}',t)]$ ($\alpha,\beta = 1$–4). The detunings are, respectively, given by $\Delta_2 = \omega_{p1}-\omega_{p2}-(E_2-E_1)/\hbar = -(E_2-E_1)/\hbar$ (because $\omega_{p1}=\omega_{p2}=\omega_p$), $\Delta_3 = \omega_p-(\omega_3-\omega_1)$, and $\Delta_4 = \omega_p+\omega_c-(\omega_4-\omega_1)$, with $E_\alpha = \hbar\omega_\alpha$ the eigenenergy of atomic state $|\alpha\rangle$. The half Rabi frequencies of the probe and control fields are, respectively, defined by $\Omega_{p1} = (\hat{\mathbf{e}}_{p+}\cdot\mathbf{p}_{31})\mathcal{E}_{p+}/\hbar$, $\Omega_{p2} = (\hat{\mathbf{e}}_{p-}\cdot\mathbf{p}_{32})\mathcal{E}_{p-}/\hbar$, and $\Omega_c = (\hat{\mathbf{e}}_c\cdot\mathbf{p}_{43})\mathcal{E}_c/\hbar$, with $\mathbf{p}_{\alpha\beta}$ the electric-dipole matrix element associated with the transition between $|\alpha\rangle$ and $|\beta\rangle$. The last term on the right-hand side of Eq. (1) is contributed by the Rydberg-Rydberg interaction with the vdW potential of the form $\hbar\mathcal{V}(\mathbf{r}'-\mathbf{r}) = -\hbar C_6/|\mathbf{r}'-\mathbf{r}|^6$ (C_6 is a dispersion parameter).

The dynamics of the atoms is controlled by the Heisenberg equation of motion for the atomic operators $\hat{S}_{\alpha\beta}(\mathbf{r},t)$, i.e., $i\hbar\frac{\partial}{\partial t}\hat{S}_{\alpha\beta}(\mathbf{r},t) = [\hat{H},\hat{S}_{\alpha\beta}(\mathbf{r},t)]$. Taking expectation values on both sides of this equation, we obtain the optical Bloch equation involving one- and two-body reduced density matri-

ces, which can be cast into the form

$$\frac{\partial \rho}{\partial t} = -\frac{i}{\hbar}[\hat{H}_0, \rho] - \Gamma[\rho] + \hat{R}[\rho_{\text{twobody}}]. \tag{2}$$

Here $\rho(\mathbf{r}, t)$ is a reduced one-body density matrix (DM) in the single-particle basis $\{|1\rangle, |2\rangle, |3\rangle, |4\rangle\}$, with the matrix elements defined by $\rho_{\alpha\beta}(\mathbf{r}, t) \equiv \langle \hat{S}_{\alpha\beta}(\mathbf{r}, t)\rangle$ [38]; $\hat{H}_0 = \mathcal{N}_a \int d^3r\, \hat{\mathcal{H}}_0(\mathbf{r}, t)$ is the Hamiltonian in the absence of the Rydberg-Rydberg interaction; Γ is a 4×4 relaxation matrix describing the spontaneous emission and dephasing. Due to the existence of the Rydberg-Rydberg interaction, a two-body reduced DM [i.e., ρ_{twobody} with DM elements $\rho_{\alpha\beta,\mu\nu}(\mathbf{r}', \mathbf{r}, t)$] is involved in this equation, represented by the last term $\hat{R}[\rho_{\text{twobody}}]$, with $\hat{R}$ a matrix denoting the contribution from the Rydberg-Rydberg interaction. Explicit expressions of Eq. (2) and a more detailed discussion on it are presented in Appendix A.

From Eq. (2) we see that, due to the Rydberg-Rydberg interaction, the evolution of one-body DM elements $\rho_{\alpha\beta}(\mathbf{r}, t)$ involves two-body DM elements $\rho_{\alpha\beta,\mu\nu}(\mathbf{r}', \mathbf{r}, t) \equiv \langle \hat{S}_{\alpha\beta}(\mathbf{r}', t)\hat{S}_{\mu\nu}(\mathbf{r}, t)\rangle$. Thus, Eq. (2) is not a closed equation. To obtain the solution of the one-body DM elements $\rho_{\alpha\beta}$, we must solve the equations for the two-body DM elements $\rho_{\alpha\beta,\mu\nu}$, which, however, involve three-body DM elements $\rho_{\alpha\beta,\mu\nu,\delta\sigma}$, and so on. As a result, one obtains a hierarchy of infinite equations for N-body DM elements (also called N-body correlators; $N = 1, 2, 3, \ldots$) that must be solved simultaneously. To make the problem solvable, a consistent and effective approach on such a hierarchy of infinite equations involving various orders of many-body correlators is needed. A powerful technique for such an approach is the reduced density matrix expansion, by which the hierarchy of the infinite equations is truncated consistently, and the problem can be reduced to solve the closed equations for the one- and two-body DM elements [see Eq. (A3)], as shown recently [12,14].

The probe field is governed by the Maxwell equation $\nabla^2\mathbf{E} - (1/c^2)\partial^2\mathbf{E}/\partial t^2 = [1/(\varepsilon_0 c^2)]\partial^2\mathbf{P}/\partial t^2$, with $\mathbf{P} = \mathcal{N}_a \sum_{j=1}^{2} \mathbf{p}_{j3}\rho_{3j} \exp[i(\mathbf{k}_{p\pm} \cdot \mathbf{r} - \omega_p t)] + \text{c.c.}$ the electric-polarization intensity. Under paraxial and slowly varying envelope approximations, the Maxwell equation is reduced to [7]

$$i\left(\frac{\partial}{\partial z} + \frac{1}{c}\frac{\partial}{\partial t}\right)\Omega_{pj} + \frac{c}{2\omega_p}\nabla_\perp^2\Omega_{pj} + \kappa_{j3}\rho_{3j} = 0 \tag{3}$$

for the two polarization components ($j = 1, 2$), where $\nabla_\perp^2 = \partial^2/\partial x^2 + \partial^2/\partial y^2$, $\kappa_{13} \equiv \mathcal{N}_a\omega_p|(\hat{\mathbf{e}}_{p+} \cdot \mathbf{p}_{13})|^2/(2\varepsilon_0 c\hbar)$, and $\kappa_{23} \equiv \mathcal{N}_a\omega_p|(\hat{\mathbf{e}}_{p-} \cdot \mathbf{p}_{23})|^2/(2\varepsilon_0 c\hbar)$ are coupling constants. The probe field is assumed to propagate along the z direction, i.e., $\mathbf{k}_{p\pm} = (0, 0, \omega_p/c)$. To suppress the Doppler effect, the control field is chosen to propagate along the negative z direction, i.e., $\mathbf{k}_c = (0, 0, -\omega_c/c)$.

The model described above is widely applicable as the assumptions made are fulfilled by typical Rydberg gas experiments. For the latter considerations where numerical values of system parameters are needed to obtain theoretical results numerically, here we take cold ^{87}Rb atomic gas as a realistic example. The assigned atomic levels are [39] $|1\rangle = |5S_{1/2}, F = 1, m_F = -1\rangle$, $|2\rangle = |5S_{1/2}, F = 1, m_F = 1\rangle$, $|3\rangle = |5P_{3/2}, F = 1, m_F = 0\rangle$, and $|4\rangle = |nS_{1/2}\rangle$. The parameters are $\Gamma_{13} = \Gamma_{23} = 2\pi \times 3.1$ MHz, $\Gamma_{34} = 2\pi \times 16.7$ kHz, $\Gamma_{21} = \Gamma_{12} = 2\pi \times 1.0$ kHz, $\Delta_2 = 2\pi \times 0.2$ MHz, $\Delta_3 = 2\pi \times 120$ MHz, $\Delta_4 = 2\pi \times 0.1$ MHz, $\Omega_c = 2\pi \times 13$ MHz, and $\mathcal{N}_a = 5.0 \times 10^{10}$ cm^{-3}. For principal quantum number $n = 60$, $C_6 = -2\pi \times 140$ GHz μm^6 (i.e., the Rydberg-Rydberg interaction is repulsive) [4,40].

B. Enhanced Kerr nonlinearities

Since the probe field is weak, a standard perturbation expansion developed in Refs. [12,14,41] can be applied to solve Eq. (2) by taking Ω_{pj} as small parameters. Then we can acquire the solutions of Eq. (2) up to a third-order approximation, which are given in Appendix A; in particular, the result of the one-body DM elements ρ_{31} and ρ_{32} exact to third-order approximation can be obtained analytically. With the results of ρ_{31} and ρ_{32}, we can obtain the optical susceptibility for the jth polarization component of the probe field, i.e., $\chi_j = \mathcal{N}_a(\hat{\mathbf{e}}_{p\pm} \cdot \mathbf{p}_{1j})\rho_{3j}/(\varepsilon_0\mathcal{E}_{p\pm})$, given by

$$\chi_j = \chi_j^{(1)} + \left[\chi_{j,\text{loc}}^{(3,s)} + \chi_{j,\text{nloc}}^{(3,s)}\right]|\mathcal{E}_{p\pm}|^2 + \left[\chi_{j,\text{loc}}^{(3,c)} + \chi_{j,\text{nloc}}^{(3,c)}\right]|\mathcal{E}_{p\mp}|^2, \tag{4}$$

where $\chi_j^{(1)}$, $\chi_{j,\text{loc}}^{(3,s)}$ [$\chi_{j,\text{loc}}^{(3,c)}$], and $\chi_{j,\text{nloc}}^{(3,s)}$ [$\chi_{j,\text{nloc}}^{(3,c)}$] are linear susceptibility, local self-Kerr (cross-Kerr) nonlinear susceptibility, and nonlocal self-Kerr (cross-Kerr) nonlinear susceptibility, respectively. The explicit expressions of these susceptibilities are presented in Appendix B.

Using the system parameters given in the preceding subsection, we obtain $\chi_{j,\text{loc}}^{(3,s)} \approx \chi_{j,\text{loc}}^{(3,c)} = (5.81 + 0.46i) \times 10^{-12}$ m^2 V^{-2} and $\chi_{j,\text{nloc}}^{(3,s)} \approx \chi_{j,\text{nloc}}^{(3,c)} = (-6.31 + 0.21i) \times 10^{-9}$ m^2 V^{-2}. We see that (i) the real parts of all the optical Kerr susceptibilities are much larger than their corresponding imaginary parts, which is due to the double EIT effect induced by the control field; (ii) the nonlocal Kerr nonlinear susceptibilities are much larger (around three orders of magnitude) than the local Kerr nonlinear susceptibilities. The reason for this is that the strong atom-atom interaction contributed by the Rydberg excitations plays a dominant role over the photon-atom interaction to the nonlinear optical polarization in the system [12,14].

C. Coupled nonlocal NLS equations

With the results of ρ_{31} and ρ_{32} obtained by the perturbation expansion exact to the third-order approximation, coupled envelope equations controlling the dynamics of the two polarization components of the probe field can be derived from the Maxwell Eq. (3), which read

$$i\frac{\partial \Omega_{pj}}{\partial z} + \frac{c}{2\omega_p}\nabla_\perp^2\Omega_{pj} + \sum_{l=1}^{2} W_{jl}|\Omega_{pl}|^2\Omega_{pj} + \sum_{l=1}^{2}\int d^2r'\mathcal{N}'_{jl}(\mathbf{r}'_\perp - \mathbf{r}_\perp)|\Omega_{pl}(\mathbf{r}'_\perp, z)|^2\Omega_{pj}(\mathbf{r}_\perp, z) = 0 \tag{5}$$

for the two polarization components ($j = 1, 2$), where $d^2r' = dx'dy'$. Note that, when deriving the above equations, we have assumed that the probe field is a spatial light beam, i.e., its envelopes are stationary (i.e., Ω_{pj} is time-independent everywhere). Such an assumption is valid for the probe field

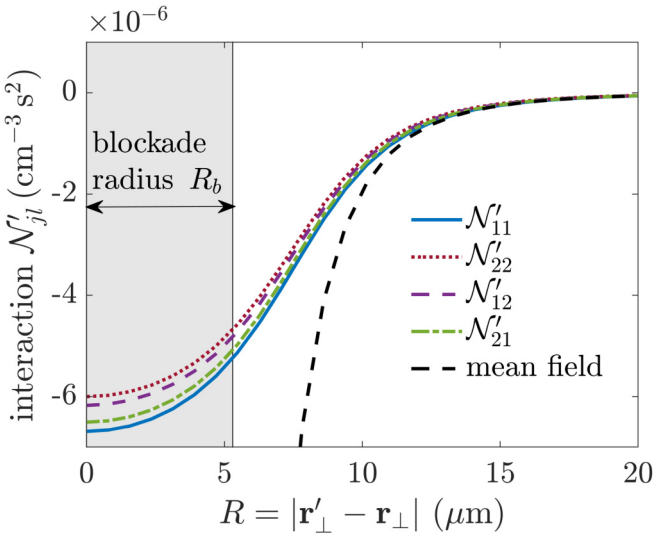

FIG. 2. Effective nonlinear interaction potentials between photons $\mathcal{N}'_{jl}$ as functions of the separation $R = |\mathbf{r}'_\perp - \mathbf{r}_\perp|$. Curves illustrated, respectively, by solid blue, dotted red, dashed purple, and dotted-dashed green lines are for $\mathcal{N}'_{11}$, $\mathcal{N}'_{22}$, $\mathcal{N}'_{12}$, and $\mathcal{N}'_{21}$, which are approach finite values when $R \to 0$. For comparison, the result obtained by using the mean-field approximation is also shown (dashed black line), which diverges rapidly when R becomes small. The shadow region on the left-hand side is the one for small interatomic distance, where the effective interaction tends to be finite and saturated due to the atomic correlations.

having a large time duration, so that a continuous-wave (CW) approximation can be applied [7,8,16]; moreover, the spatial width of the envelopes in the z direction is assumed to be large so that a local approximation in the z direction for the *effective* nonlinear interaction potentials between photons [7,8,14,16] (or called spatial response functions) $\mathcal{N}_{jl}(\mathbf{r}' - \mathbf{r})$ can be made, which gives $\int_{-\infty}^{+\infty} \mathcal{N}_{jl}(\mathbf{r}' - \mathbf{r})dz' = \mathcal{N}'_{jl}(\mathbf{r}'_\perp - \mathbf{r}_\perp)$. For a detailed derivation of the coupled 3D NNLS equations (5), see the Appendix B.

Shown in Fig. 2 are $\mathcal{N}'_{jl}$ as functions of the interatomic separation $R = |\mathbf{r}'_\perp - \mathbf{r}_\perp|$, calculated by using the parameters given in Sec. II A. Curves plotted by solid blue, dotted red, dashed purple, and dotted-dashed green lines are for $\mathcal{N}'_{11}$, $\mathcal{N}'_{22}$, $\mathcal{N}'_{12}$, and $\mathcal{N}'_{21}$, respectively. We see that all four nonlinear response functions approach finite values for small R (indicated by the shadow region on the left-hand side of the figure). This is contributed from the Rydberg-Rydberg interaction that induces strong correlations between the atoms and causes the effective interaction potentials between photons to be saturated for small R. In the figure, the region of the Rydberg blockade (with radius R_b) for the atom-atom interaction is indicated by the shadow one. For comparison, the result obtained by using a mean-field approximation is also shown in the figure (see the dashed black line), which is divergent for small R due to the improper neglect of the atomic correlations in such a calculation.

Since the local Kerr nonlinear susceptibilities are much smaller than the nonlocal ones, the third term on the left side of Eq. (5) plays no significant role and can be safely neglected. For the convenience of the following physical discussions and numerical simulations, we recast Eq. (5) into the dimensionless form

$$i\frac{\partial u_j}{\partial s} + \tilde{\nabla}_\perp^2 u_j + \sum_{l=1,2} \int d^2\zeta' [\Re_{jl}(\vec{\zeta}' - \vec{\zeta})|u_l(\vec{\zeta}', s)|^2] u_j(\vec{\zeta}, s) = 0, \quad (6)$$

where $u_j = \Omega_{pj}/U_0$, $s = z/(2L_{\rm diff})$, $\tilde{\nabla}_\perp^2 = \partial^2/\partial\xi^2 + \partial^2/\partial\eta^2$, $\vec{\zeta} = (\xi, \eta) = (x, y)/R_0$, $d^2\zeta' = d\xi' d\eta'$, and $\Re_{jl}(\vec{\zeta}' - \vec{\zeta}) = 2L_{\rm diff}R_0^2U_0^2\mathcal{N}'_{jl}[(\vec{\zeta}' - \vec{\zeta})R_0]$ [42], with U_0, $L_{\rm diff} \equiv \omega_p R_0^2/c$, and R_0 typical half Rabi frequency, diffraction length, and transverse size (e.g., the lattice separation of optical patterns) of the probe field, respectively [43]. Equations (6) can be cast into the form

$$i\frac{\partial v_j}{\partial s} + \tilde{\nabla}_\perp^2 v_j + \sum_{l=1,2} \int d^2\zeta' [I_l \Re_{jl}(\vec{\zeta}' - \vec{\zeta})|v_l(\vec{\zeta}', s)|^2] v_j(\vec{\zeta}, s) = 0, \quad (7)$$

where $I_j = \int |u_j(\vec{\zeta})|^2 d^2\zeta$ is the power of the jth polarization component; $v_j(\vec{\zeta}) = u_j(\vec{\zeta})/I_j^{1/2}$, which satisfies the normalization condition $\int |v_j(\vec{\zeta})|^2 d^2\zeta = 1$. The property of the reduced response functions $\Re_{jl}$ depends significantly on the *nonlocality degree* of the Kerr nonlinearity, defined by

$$\sigma \equiv R_b/R_0. \quad (8)$$

Here R_b is the blockade radius of the Rydberg blockade sphere, given by $R_b = |C_6/\delta_{\rm EIT}|^{1/6}$ [6,7], with $\delta_{\rm EIT}$ the width of the EIT transparency window. One has $\delta_{\rm EIT} = |\Omega_c|^2/\gamma_{31}$ for $\Delta_3 = 0$, and $\delta_{\rm EIT} = |\Omega_c|^2/\Delta_3$ for $\Delta_3 \gg \gamma_{31}$. With the system parameters used here, we have $R_b \approx 5.40$ μm. The value of σ can be varied by changing R_0, used in the following calculations.

III. MODULATION INSTABILITY, PATTERN FORMATION, PHASE SEPARATION, SOLITONS, AND VORTICES

A. Modulation instability for the two polarization components of the probe field

We now consider the MI and related pattern formation that may occur in the system based on the coupled NNLS equations obtained above. MI is a nonlinear instability of constant-amplitude continuous waves under the influence of small perturbations, occurring in a variety of contexts where Kerr nonlinearities are attractive and local [44,45]; it can also arise in systems with repulsive but nonlocal Kerr nonlinearity when the perturbations have both long [46,47] and short [8,30] wavelengths.

To explore the MI in the present system, we consider the plane-wave solution of the coupled NNLS Eq. (7), i.e., $v_{{\rm pw},j}(\vec{\zeta}, s) = v_{j0}\exp(i\mu_j s)$ with $\mu_j = \iint d^2\zeta [I_j v_{10}^2 \Re_{jj}(\vec{\zeta}) + I_{3-j} v_{20}^2 \Re_{3-j,j}(\vec{\zeta})]$ $(j = 1, 2)$. Since any perturbation can be expanded as a superposition of many Fourier modes, the modulation of the plane-wave solution by the perturbation can be cast into the form

$$\tilde{v}_j(\vec{\zeta}, s) = [v_{j0} + a_{1j}e^{i\vec{\beta}\cdot\vec{\zeta} + \lambda s} + a_{2j}^* e^{-i\vec{\beta}\cdot\vec{\zeta} + \lambda^* s}]e^{i\mu_j s}, \quad (9)$$

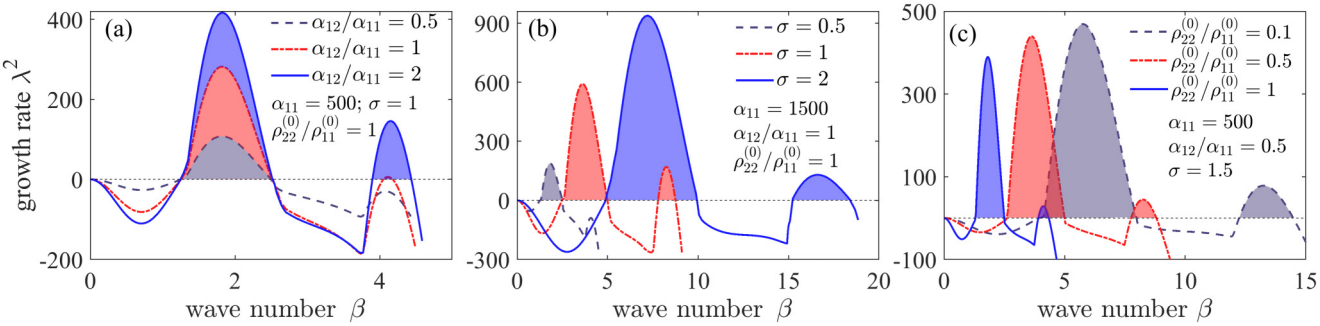

FIG. 3. Growth rate of the MI for the two-component plane-wave probe field as a function of the dimensionless wave number $\beta = \sqrt{\beta_1^2 + \beta_2^2}$ [$\beta_1 \equiv R_0 k_x$, $\beta_2 \equiv R_0 k_y$] for different nonlinearity parameters α_{jl} [defined in Eq. (11), with $\alpha_{11} = \alpha_{22}$, $\alpha_{12} = \alpha_{21}$] and the nonlocality degree $\sigma = R_b/R_0$ of the Kerr nonlinearities. Here k_x, k_y are, respectively, wave numbers in the x and y directions; R_0 and R_b are, respectively, the typical transverse beam radius of the probe field and the radius of the Rydberg blockade sphere. (a) λ^2 as a function of β for the cross-Kerr nonlinearity parameter $\alpha_{12} = 0.5\,\alpha_{11}$ (dashed gray line), $\alpha_{12} = \alpha_{11}$ (dotted red line), and $\alpha_{12} = 2\,\alpha_{11}$ (solid blue line), respectively. Here $\sigma = 1$, $\alpha_{11} = 500$, and $\rho_{22}^{(0)}/\rho_{11}^{(0)} = 1$ ($\rho_{11}^{(0)}$ and $\rho_{22}^{(0)}$ are the initial populations at the two atomic ground states) are assumed. (b) λ^2 as a function of β for the nonlocality degree of the Kerr nonlinearities $\sigma = 0.5$ (dashed gray line), $\sigma = 1$ (dotted red line), and $\sigma = 2$ (solid blue line), respectively. Here $\alpha_{11} = 1500$, $\alpha_{12} = \alpha_{11}$, and $\rho_{22}^{(0)}/\rho_{11}^{(0)} = 1$ are assumed. (c) λ^2 as a function of β for $\rho_{22}^{(0)}/\rho_{11}^{(0)} = 0.1$ (dashed gray line), $\rho_{22}^{(0)}/\rho_{11}^{(0)} = 0.5$ (dotted red line), and $\rho_{22}^{(0)}/\rho_{11}^{(0)} = 1$ (solid blue line), respectively. Here $\alpha_{11} = 500$, $\alpha_{12} = 0.5\alpha_{11}$, and $\sigma = 1.5$ are assumed. Colorful regions in all the panels are ones for $\Re(\lambda) > 0$, where MI occurs and hence the two-component plane-wave probe field is unstable [48].

where a_{1j} and a_{2j} are small complex amplitudes of the perturbation, $\vec{\beta} = (\beta_1, \beta_2)$ ($\beta_1 \equiv R_0 k_x$, $\beta_2 \equiv R_0 k_y$; k_x, k_y are wave numbers in the x and y directions, respectively) is a dimensionless 2D wave vector, and λ is the growth rate of the perturbation.

Substituting the perturbation solution (9) into Eqs. (7) and keeping only linear terms of a_{1j} and a_{2j}, we can obtain $\lambda = \lambda_\pm$. The result is given by

$$\lambda_\pm^2 = \beta^2 A_+ - \beta^4 \pm \beta^2 \sqrt{A_-^2 + 4 I_1 I_2 \tilde{\Re}_{12}(\vec{\beta}) \tilde{\Re}_{21}(\vec{\beta})}, \tag{10}$$

where $A_\pm = I_1 \tilde{\Re}_{11}(\vec{\beta}) \pm I_2 \tilde{\Re}_{22}(\vec{\beta})$, $\beta = \sqrt{\beta_1^2 + \beta_2^2}$, and $\tilde{\Re}_{jl}(\vec{\beta})$ is the response function in momentum space [i.e., the Fourier transformation of $\Re_{jl}(\vec{\zeta})$]. We find the growth rate λ has four branches, i.e., $\lambda_{+(1,2)}$ and $\lambda_{-(1,2)}$, in which only the positive branch can result in MI. The property of λ depends on the power of the input probe fields I_j and the shape of the response function $\tilde{\Re}_{jl}$. For convenience, we define the *nonlinearity parameters*

$$\alpha_{jl} = I_l \int \Re_{jl}(\vec{\zeta}) d^2\zeta. \tag{11}$$

Due to the symmetry of the inverted Y-type level structure considered here [Fig. 1(a)], if $I_1 = I_2$ one has approximately $\alpha_{11} = \alpha_{22}$ and $\alpha_{12} = \alpha_{21}$. Other cases for $I_1 \neq I_2$ may give very rich behaviors of the pattern formation for the two polarized components of the probe field. In this work, for simplicity, we discuss only the particular case $I_1 = I_2$.

The MI can be controlled by manipulating the physical parameters of the system. Figure 3 shows λ^2 as a function of the dimensionless wave number β for different nonlinearity parameters α_{jl}, the nonlocality degree σ, and the *ratio of initial populations* prepared in two atomic ground states, i.e., $\rho_{22}^{(0)}/\rho_{11}^{(0)}$ [48]. Plotted in Fig. 3(a) is the curve of λ^2 as a function of β for the cross-Kerr nonlinearity parameter $\alpha_{12} = 0.5\,\alpha_{11}$ (dashed gray line), $\alpha_{12} = \alpha_{11}$ (dotted red line), and $\alpha_{12} = 2\,\alpha_{11}$ (solid blue line), respectively (here $\sigma = 1$, $\alpha_{11} = 500$, and $\rho_{22}^{(0)}/\rho_{11}^{(0)} = 1$ are assumed). We see that the MI may happen in different domains of the wave number β. The reason for the appearance of the second MI domain stems from the cross-Kerr nonlinearity of the system.

The nonlocality degree of the Kerr nonlinearities can also be used to control the MI. Figure 3(b) shows λ^2 as a function of wave number β for the nonlocality degree $\sigma = 0.5$ (dashed gray line), $\sigma = 1$ (dotted red line), and $\sigma = 2$ (solid blue line), respectively (here $\alpha_{11} = 1500$, $\alpha_{12} = \alpha_{11}$, and $\rho_{22}^{(0)}/\rho_{11}^{(0)} = 1$ are assumed). In this case the MI domain is significantly modified when σ is varied, which is quite different from those modifications induced by the Kerr nonlinearities illustrated in Fig. 3(a); furthermore, the critical wave number for the appearance of the MI is also enlarged greatly.

The populations initially prepared in the two atomic ground states $|1\rangle$ and $|2\rangle$ (i.e., $\rho_{11}^{(0)}$, $\rho_{22}^{(0)}$) also play an important role for the appearance of the MI. Plotted in Fig. 3(c) is λ^2 as a function of β for the ratio of the populations $\rho_{22}^{(0)}/\rho_{11}^{(0)} = 0.1$ (dashed gray line), $\rho_{22}^{(0)}/\rho_{11}^{(0)} = 0.5$ (dotted red line), and $\rho_{22}^{(0)}/\rho_{11}^{(0)} = 1$ (solid blue line), respectively (here $\alpha_{11} = 500$, $\alpha_{12} = 0.5\alpha_{11}$, and $\sigma = 1.5$ are assumed). In this situation, the MI domain is dramatically changed when $\rho_{22}^{(0)}/\rho_{11}^{(0)}$ is varied; moreover, the critical wave number for the appearance of the MI decreases with the increase of $\rho_{22}^{(0)}/\rho_{11}^{(0)}$.

From these results we see that the MI depends not only on the nonlinearity parameters (α_{jl}), but also on the nonlocality degree of Kerr nonlinearities (σ) as well as the population initially prepared in the two atomic ground states ($\rho_{22}^{(0)}/\rho_{11}^{(0)}$). This provides many ways to manipulate the MI and thereby the optical patterns in the system, discussed in the next subsections.

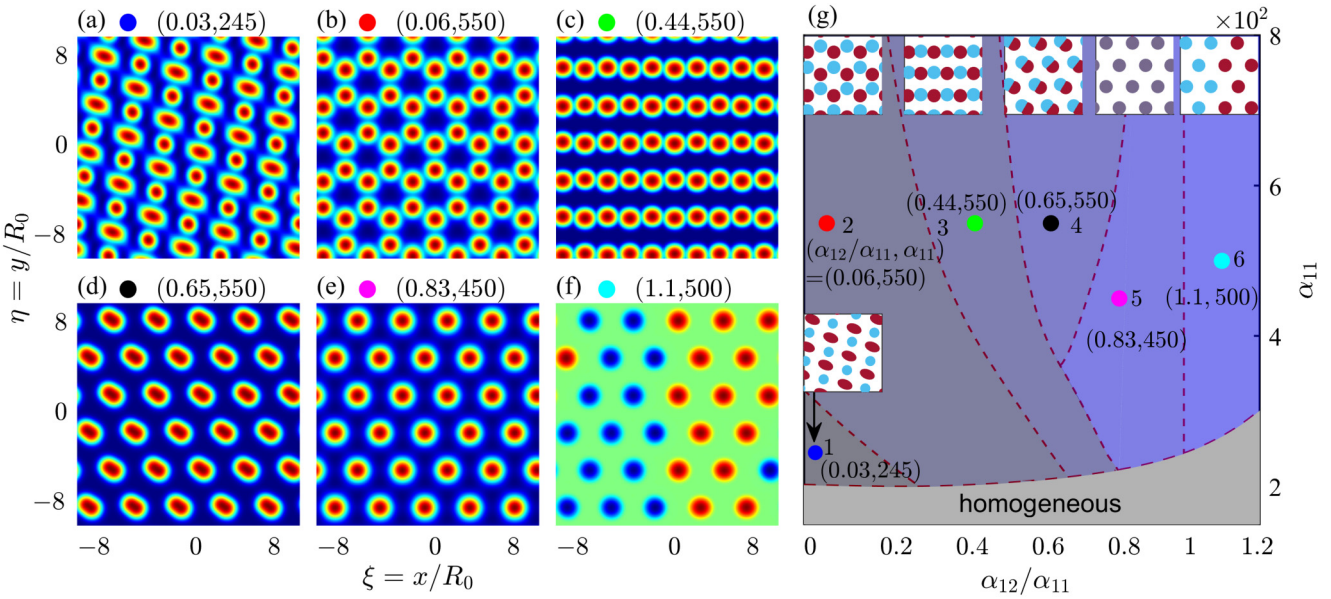

FIG. 4. Pattern formation of the two-component probe field controlled by the nonlinearity parameters α_{11} and α_{12}, by taking the dimensionless normalized probe-field intensity $|v|^2 \equiv |v_1|^2 + |v_2|^2$ as a function of the dimensionless coordinates $\xi = x/R_0$ and $\eta = y/R_0$ (with $\sigma = 1$ and $\rho_{22}^{(0)}/\rho_{11}^{(0)} = 1$) for different nonlinearity parameters: (a) $(\alpha_{12}/\alpha_{11}, \alpha_{11}) = (0.03, 245)$; (b) $(\alpha_{12}/\alpha_{11}, \alpha_{11}) = (0.06, 550)$; (c) $(\alpha_{12}/\alpha_{11}, \alpha_{11}) = (0.44, 550)$; (d) $(\alpha_{12}/\alpha_{11}, \alpha_{11}) = (0.65, 550)$; (e) $(\alpha_{12}/\alpha_{11}, \alpha_{11}) = (0.83, 450)$; (f) $(\alpha_{12}/\alpha_{11}, \alpha_{11}) = (1.1, 550)$. In the figure, the region with a brighter (darker) color means that the light intensity in that region is higher (lower). (g) Phase diagram for the optical pattern formation, in which different domains (phases) are obtained by using different values of $(\alpha_{12}/\alpha_{11}, \alpha_{11})$ corresponding, respectively, to those used in (a)–(f). The inserted schematics in each domain stands for the optical pattern obtained with the indicated value of $(\alpha_{12}/\alpha_{11}, \alpha_{11})$, where the distributions of two probe-field components are illustrated by the solid blue circles (denoting $|v_1|^2$) and solid red circles (denoting $|v_2|^2$), respectively. Large solid circles with different colors in six domains (with numbers 1, 2, 3, 4, 5, 6 indicated, respectively) of the phase diagram are used to guide the look for the correspondence between different phases and different optical patterns given in (a)–(f), respectively. Note that a spatial phase separation occurs in the case shown in (f), where the light-intensity distributions of the two polarization components are separated in space.

B. Pattern formations controlled by the ratio between the cross- and self-Kerr nonlinearities

We now explore the outcome of the MI discussed above. To demonstrate the appearance of optical patterns, we seek the stationary-state solutions of the system, for which the total energy

$$E = \sum_{j=1}^{2} \int |\tilde{\nabla}_\perp v_j|^2 d^2\zeta + \sum_{j,l=1}^{2} E_{jl} \tag{12}$$

is minimal. Such solutions of Eq. (7) are sought in the form $v_j = v_{j0} \exp(iE_0 s)$ (with E_0 the ground-state energy), which can be obtained numerically by using an imaginary propagation together with split-step Fourier method [49] (for details, see Appendix C). In the above expression, the first term is the kinetic energy and the second term [with $E_{jl} \equiv \frac{1}{2} \int\int d^2\zeta d^2\zeta' \Re_{jl}(\vec{\zeta}' - \vec{\zeta}) |v_j(\vec{\zeta}', s)|^2 |v_l(\vec{\zeta}, s)|^2$] is the interaction energy. The initial condition used in the numerical simulation is a plane wave, perturbed by a random noise.

Due to the spontaneous symmetry breaking induced by the MI, the plane-wave state of the system is transferred into new states, manifested by the emergence of structured optical patterns. Figure 4 shows the optical patterns [Figs. 4(a)–4(f)] and the related phase diagram [Fig. 4(g), where "homogeneous" means the plane-wave state] of the two-component probe field controlled by the nonlinearity parameters α_{11} and α_{12} [α_{jl} is defined in Eq. (11)], by taking the dimensionless, normalized field intensity $|v|^2 \equiv |v_1|^2 + |v_2|^2$ [50] as a function of the dimensionless coordinates $\xi = x/R_0$ and $\eta = y/R_0$ (with $\sigma = 1$ and $\rho_{22}^{(0)}/\rho_{11}^{(0)} = 1$). In Figs. 4(a)–4(f), the region with brighter (darker) color means that the light intensity in that region is higher (lower). For convenience, in each domain of Fig. 4(g) an insertion is provided to distinguish the distributions $|v_1|^2$ and $|v_2|^2$, denoted by solid blue and red circles, respectively.

Shown in Fig. 4(a) is the optical pattern for the case of $(\alpha_{12}/\alpha_{11}, \alpha_{11}) = (0.03, 245)$, where the circular and elliptical spots are for the v_1 (i.e., σ^+) and v_2 (i.e., σ^-) polarization components, respectively. We see that both the v_1 and v_2 components form hexagonal lattices, which are located at different positions. An obvious feature is that the spots of the v_2-component are elliptical, but those of the v_1-component are circular. The reason for the appearance of such a phenomenon is that the v_1-component gives a hexagonal lattice structure with circular bright spots (where light intensity is maximal) in a dark background, while the v_2-component gives a hexagonal lattice structure but with circular dark spots (where light intensity is minimal) in a bright background. As a result, the intensity superposition of the two polarized components (i.e., $|v_1|^2 + |v_2|^2$) gives an optical pattern in which the circular and elliptical spots appear alternatively in space. For details, see Appendix D. This case corresponds to the domain 1 of the phase diagram given in Fig. 4(g).

Figure 4(b) shows the result for $(\alpha_{12}/\alpha_{11}, \alpha_{11}) = (0.06, 550)$. The optical patterns for both the v_1 and v_2 components obtained here are also hexagonal lattices, but their superposition $|v_1|^2 + |v_2|^2$ forms a honeycomb lattice, i.e., one circular spot of one component is surrounded by three circular spots of the other component. This situation is relevant to the domain 2 in the phase diagram shown by Fig. 4(g). As an example, we also show the formation process of the hexagonal lattices for v_1 and v_2 components and the honeycomb lattice of their superposition $|v_1|^2 + |v_2|^2$ via the MI starting from an inhomogeneous plane-wave state; see Figs. 1(c1)–1(c3), where (c1) [(c2)] represents the σ^+ (σ^-) polarization component and (c3) represents their superposition (i.e., the total probe field) for different propagation distance z.

The ratio of nonlinearity α_{12}/α_{11} plays an important role for forming different optical structures. To test this idea, we increase α_{12} to make the nonlinearity parameters adjusted to be $(\alpha_{12}/\alpha_{11}, \alpha_{11}) = (0.44, 550)$. In this case, a different optical structure emerges in the system, as illustrated in Fig. 4(c), where two hexagonal lattices (each consisting of circular spots) are staggered and they form a square lattice pattern for their superposition $|v_1|^2 + |v_2|^2$. This case corresponds to the domain 3 of the phase diagram given in Fig. 4(g).

Shown in Figs. 4(d) and 4(e) are $(\alpha_{12}/\alpha_{11}, \alpha_{11})$ equaling $(0.65, 550)$ and $(0.83, 450)$, respectively. Both cases still give hexagonal lattice patterns; the lattice spots in Fig. 4(d) are elliptical, while the lattice spots in Fig. 4(e) are circular. The reason is that in Fig. 4(d) the lattice-point positions of the v_1-component have a small separation from those of the v_2-component, while in Fig. 4(e) the lattice-point positions of the v_1-component coincide with those of the v_2-component. This point can be clearly seen from the phase diagram of these two cases [i.e., the domains 4 and 5 of Fig. 4(g)], where the light-intensity distributions of $|v_1|^2$ and $|v_2|^2$ have been given by the inserted schematics.

Interestingly, when the cross-Kerr nonlinearity is increased further, i.e., $(\alpha_{12}/\alpha_{11}, \alpha_{11}) = (1.1, 500)$, an optical phase separation occurs in the system, as shown by Fig. 4(f), where the light-intensity distributions of $|v_1|^2$ (displayed by solid blue circles) and $|v_2|^2$ (displayed by solid red circles) are separated in space, which is relevant to the domain 6 in Fig. 4(g). Such a phase separation phenomenon is very similar to that occurring in a mixture of binary fluids [51–60]. We shall discuss this topic in more detail in Sec. III E.

C. Pattern formations controlled by the nonlocality degree of the Kerr nonlinearities

The nonlocality degree of Kerr nonlinearities can also be used to manipulate the MI [see Fig. 3(b)], trigger symmetry breaking, and generate different optical patterns in the system. Similar to the last subsection, one can find the stationary-state distributions of the probe field [for which the total energy (12) is minimal] through a numerical simulation on Eq. (7) for different values of the nonlocality degree of Kerr nonlinearities. Figure 5 shows the optical patterns [Figs. 5(a)–5(f)] and the related phase diagram [Fig. 5(g)] of the two-component probe field controlled by the ratio of nonlinearity α_{12}/α_{11} and the nonlocality degree σ by taking $|v_1|^2 + |v_2|^2$ as a function of $\xi = x/R_0$ and $\eta = y/R_0$ (with $\alpha_{11} = 550$ and $\rho_{22}^{(0)}/\rho_{11}^{(0)} = 1$). Similar to Fig. 4(g), in each domain of Fig. 5(g), an insertion is given for distinguishing the distributions $|v_1|^2$ (denoted by solid blue circles) and $|v_2|^2$ (denoted by solid red circles).

Plotted in Fig. 5(a) is the intensity distribution $|v_1|^2 + |v_2|^2$ of the optical pattern for the case of $(\alpha_{12}/\alpha_{11}, \sigma) = (0.1, 1.1)$. We see that both the v_1 and v_2 components form hexagonal lattices, locating at different positions, but the circular and elliptical spots are for the v_1 (i.e., σ^+) and v_2 (i.e., σ^-) polarization components, respectively, which is similar to that of Fig. 4(a) (see the explanation given in Appendix D). This case corresponds to the domain 1 of the phase diagram given in Fig. 5(g).

Shown in Fig. 5(b) is the result for $(\alpha_{12}/\alpha_{11}, \sigma) = (0.3, 1.2)$, which is similar to that in Fig. 4(b). The optical patterns for both the v_1 and v_2 components obtained are also hexagonal lattices, but their superposition $|v_1|^2 + |v_2|^2$ forms a honeycomb lattice. This situation is relevant to the domain 2 in the phase diagram shown by Fig. 5(g).

Compared to Fig. 5(b), a different optical structure emerges for $(\alpha_{12}/\alpha_{11}, \sigma) = (0.3, 0.4)$, as shown in Fig. 5(c). Here two hexagonal lattices (each consisting of circular spots) are staggered and they form a square lattice pattern for their superposition $|v_1|^2 + |v_2|^2$. This case corresponds to the domain 3 of the phase diagram given in Fig. 5(g). However, if we further reduce the nonlocality degree σ to be smaller than 0.05, no regular optical pattern appears, corresponding to the gray domain on the leftmost side of the phase diagram [Fig. 5(g)]. The reason for the disappearance of the pattern is that the interaction between photons [characterized by the response function $\Re_{jl}(\vec{\zeta}' - \vec{\zeta})$ in Eqs. (7)] becomes short-ranged, which does not support MI for the repulsive Rydberg-Rydberg interaction, and hence the formation of optical patterns is not possible.

Figures 5(d) and 5(e) show the results for the case $(\alpha_{12}/\alpha_{11}, \sigma) = (0.7, 1.2)$ and $(\alpha_{12}/\alpha_{11}, \sigma) = (0.9, 0.9)$, respectively. We see that both cases give hexagonal patterns with circular spots for the v_1 and v_2 components; the lattice spots for their superposition $|v_1|^2 + |v_2|^2$ are elliptical in Fig. 5(d), but circular in Fig. 5(e). The reason for the elliptical lattice pattern displayed in Fig. 5(d) is that the lattice-point positions of the v_1-component have a small separation from those of the v_2-component; in the case of Fig. 5(e), however, the lattice-point positions of the v_1-component coincide with those of the v_2-component. One can see this point clearly from the domains 4 and 5 of Fig. 5(g), where the light-intensity distributions of $|v_1|^2$ (solid blue circles) and $|v_2|^2$ (solid red circles) have been given by the inserted schematics.

Illustrated in Fig. 5(f) is the case $(\alpha_{12}/\alpha_{11}, \sigma) = (0.98, 1.1)$. In this situation, an optical phase separation happens, by which the light-intensity distributions of $|v_1|^2$ (displayed by solid blue circles) and $|v_2|^2$ (displayed by solid red circles) are separated in space. This situation corresponds to the domain 6 in the phase diagram given in Fig. 5(g). We see from the top part of the phase diagram that the domain of the phase separation is enlarged when the nonlocality degree σ increases. This finding tells us that, in addition to the cross-Kerr nonlinearity, the nonlocality degree of the Kerr nonlinearities can also be employed to control the optical phase separation in the system.

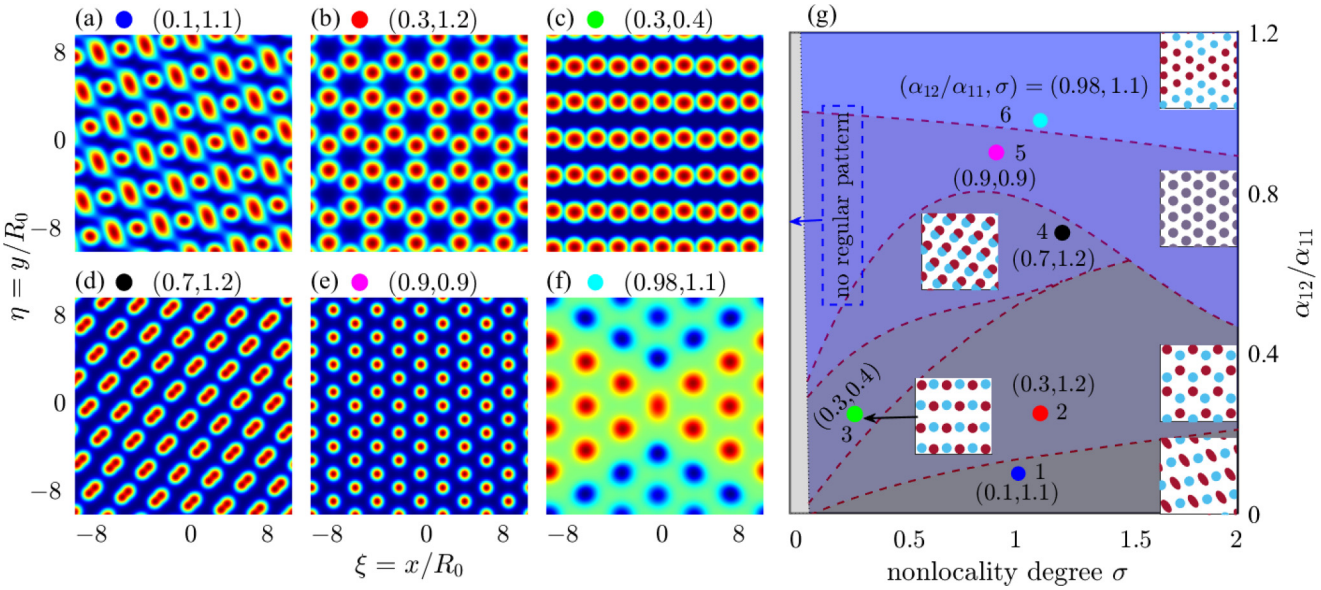

FIG. 5. Pattern formation of the two-component probe field controlled by the ratio of nonlinearity α_{12}/α_{11} and the nonlocality degree σ, by taking the dimensionless normalized probe-field intensity $|v|^2 = |v_1|^2 + |v_2|^2$ as a function of the dimensionless coordinates $\xi = x/R_0$ and $\eta = y/R_0$ (with $\alpha_{11} = 550$ and $\rho_{22}^{(0)}/\rho_{11}^{(0)} = 1$) for different α_{12}/α_{11} and σ: (a) $(\alpha_{12}/\alpha_{11}, \sigma) = (0.1, 1.1)$; (b) $(\alpha_{12}/\alpha_{11}, \sigma) = (0.3, 1.2)$; (c) $(\alpha_{12}/\alpha_{11}, \sigma) = (0.3, 0.4)$; (d) $(\alpha_{12}/\alpha_{11}, \sigma) = (0.7, 1.2)$; (e) $(\alpha_{12}/\alpha_{11}, \sigma) = (0.9, 0.9)$; (f) $(\alpha_{12}/\alpha_{11}, \sigma) = (0.98, 1.1)$. (g) Phase diagram for the optical pattern formation, in which different domains (phases) are obtained by using different values of $(\alpha_{12}/\alpha_{11}, \sigma)$ corresponding, respectively, to those used in (a)–(f). The inserted schematics in each domain stands for the optical pattern obtained with the indicated value of $(\alpha_{12}/\alpha_{11}, \sigma)$, where the distributions of two probe-field components are illustrated by the solid blue circles (denoting $|v_1|^2$) and solid red circles (denoting $|v_2|^2$), respectively. Large solid circles with different colors in six domains (with numbers 1, 2, 3, 4, 5, 6 indicated, respectively) of the phase diagram are used to look for the correspondence between different phases and different optical patterns given in (a)–(f), respectively. A spatial phase separation occurs in the case shown in (f), where the distributions of the two polarization components are separated in space (the solid blue circles are for $|v_1|^2$ and the solid red circles are for $|v_2|^2$). Note that no regular pattern occurs in the thin domain (gray color) on the leftmost side of (g) where σ is very small (i.e., about $\sigma < 0.05$).

D. Pattern formations controlled by the initial populations in the two atomic ground states

We now explore what will happen when the preparations of the initial populations in the two atomic ground states are changed. The initial populations in the ground states $|1\rangle$ and $|2\rangle$ [see Fig. 1(a)] are, respectively, given by $\rho_{11}^{(0)}$ and $\rho_{22}^{(0)}$; except for the normalized condition (i.e., $\rho_{11}^{(0)} + \rho_{22}^{(0)} = 1$), they are quite arbitrary. In the above discussions, we have taken $\rho_{22}^{(0)}/\rho_{11}^{(0)} = 1$ (i.e., $\rho_{11}^{(0)} = \rho_{22}^{(0)} = 0.5$) for simplicity. Because different initial populations can be prepared experimentally (e.g., by optical pumping or applying a microwave field to couple $|1\rangle$ and $|2\rangle$), one can use different preparations of the initial populations to control the MI [see Fig. 3(c)] and hence to create new optical patterns in the system.

We consider a general case by assuming the initial populations in the ground states $|1\rangle$ and $|2\rangle$ can be adjusted arbitrarily (with $\sigma = 1.5$ and $\alpha_{11} = 500$ fixed). As done above, we look for the stationary states of the system through numerically solving Eq. (7) under the condition of minimum energy. Figure 6 shows the optical patterns [Figs. 6(a)–6(f)] and the related phase diagram [Fig. 6(g)] of the two-component probe field.

Illustrated in Figs. 6(a)–6(c) are, respectively, the intensity distributions $|v_1|^2$, $|v_2|^2$, and $|v_1|^2 + |v_2|^2$ as functions of $\xi = x/R_0$ and $\eta = y/R_0$ by taking $(\rho_{22}^{(0)}/\rho_{11}^{(0)}, \alpha_{12}/\alpha_{11}) = (0.05, 0.5)$ (with the other parameters the same as those used in Fig. 5). One sees that a new type of optical structure appears in the system. The pattern for the v_1-component is a hexagonal lattice consisting of bright circular spots [small, solid yellow circles; see Fig. 6(a)], while the pattern for the v_2-component is very different, in which there is a bright background with inserted low-intensity hexagonal optical spots [large, solid blue circles; see Fig. 6(b)]. The superposition of the two components, i.e., $|v_1|^2 + |v_2|^2$, is displayed as a hexagonal lattice with the spots of dark circular rings [Fig. 6(c)]. This situation is relevant to the domain 1 in the phase diagram shown by Fig. 6(g).

Another type of optical structure can be found when the population in the ground state $|2\rangle$ is increased, by taking $(\rho_{22}^{(0)}/\rho_{11}^{(0)}, \alpha_{12}/\alpha_{11}) = (0.5, 0.5)$. The optical patterns in this case for $|v_1|^2$, $|v_2|^2$, and $|v_1|^2 + |v_2|^2$ are shown in Figs. 6(d)–6(f), respectively. We see that the distribution of the v_1-component is a hexagonal lattice consisting of small, solid yellow circles [Fig. 6(d)]; the distribution of the v_2-component is also a hexagonal lattice, but the spots of the lattice are large, yellow circular rings [Fig. 6(e)]. As a result, the superposition of the two components $|v_1|^2 + |v_2|^2$ displays an interesting hexagonal lattice consisting of two-ring spots [Fig. 6(f)]. The case considered here corresponds to the domain 2 in the phase diagram shown by Fig. 6(g).

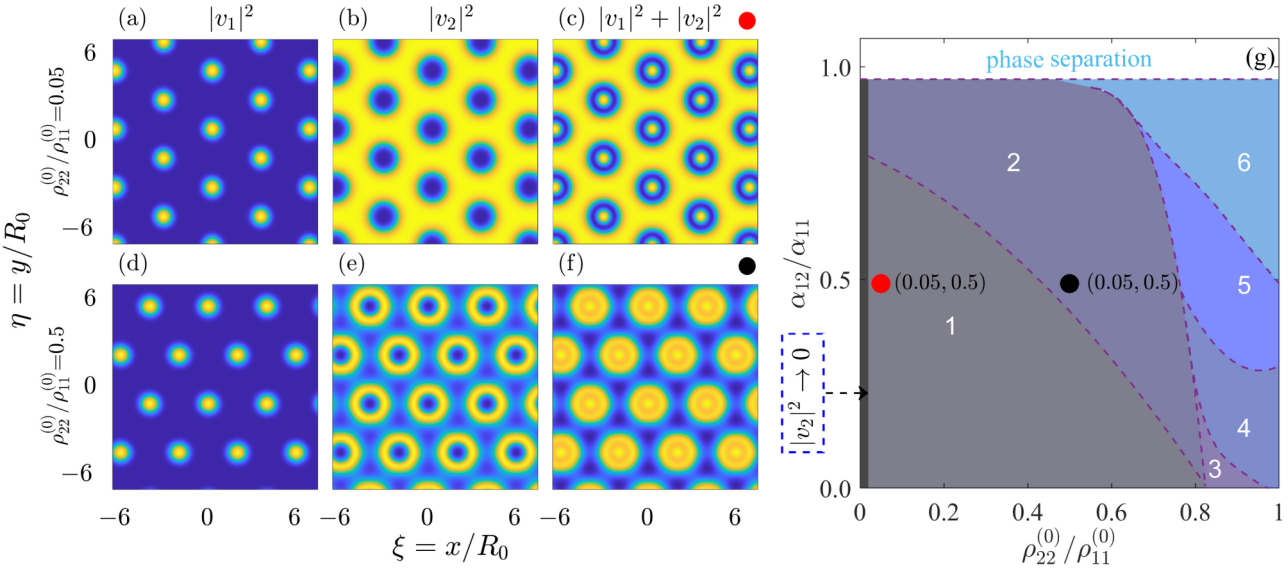

FIG. 6. Pattern formation of the two-component probe field controlled by the ratio of initial populations in the two atomic ground states $|1\rangle$ and $|2\rangle$, i.e., $\rho_{22}^{(0)}/\rho_{11}^{(0)}$, and by the ratio of nonlinearity α_{12}/α_{11}, by taking the dimensionless normalized probe-field intensity $|v|^2 = |v_1|^2 + |v_2|^2$ as a function of the dimensionless coordinates $\xi = x/R_0$ and $\eta = y/R_0$ (with $\sigma = 1.5$ and $\alpha_{11} = 500$) for different $\rho_{22}^{(0)}/\rho_{11}^{(0)}$. (a)–(c) Optical patterns of $|v_1|^2$, $|v_2|^2$, $|v_1|^2 + |v_2|^2$ for $\rho_{22}^{(0)}/\rho_{11}^{(0)} = 0.05$ and $\alpha_{12}/\alpha_{11} = 0.5$. (d)–(f) Similar to (a)–(c) but for $\rho_{22}^{(0)}/\rho_{11}^{(0)} = 0.5$ and $\alpha_{12}/\alpha_{11} = 0.5$. (g) Phase diagram for the optical pattern formation, in which different domains (phases) are obtained by using different values of $(\rho_{22}^{(0)}/\rho_{11}^{(0)}, \alpha_{12}/\alpha_{11})$. Domains 1 and 2 correspond to the optical patterns illustrated in (c) and (f), respectively. The optical patterns corresponding to domains 3–6 are similar to those of Figs. 4(b)–4(e) (omitted here). The domain on the top of (g) (white color) is the one with phase separation; the domain on the leftmost side (black color) is the one where the v_2-component disappears.

We have made further simulations on the optical pattern formation in the system by choosing other initial populations in the atomic ground states $|1\rangle$ and $|2\rangle$, with the results given in the following:

(i) When $\rho_{22}^{(0)}/\rho_{11}^{(0)} \sim 0$ (i.e., the initial populations are nearly prepared in the ground state $|1\rangle$), we find that the optical pattern occurs only for the v_1-component, which has a hexagonal-shaped structure. This case corresponds to the thin domain, with gray color shown in the leftmost side of Fig. 6(g). This is easy to understand because in this situation the system is reduced into a ladder-shaped excitation scheme (i.e., the single Rydberg-EIT involved only the atomic states $|1\rangle$, $|3\rangle$, and $|4\rangle$) when $\rho_{22}^{(0)}/\rho_{11}^{(0)} \sim 0$. Similarly, if $\rho_{11}^{(0)}/\rho_{22}^{(0)} \sim 0$, the optical pattern occurs only for the v_2-component, which has also a hexagonal-shaped structure allowed by the single Rydberg-EIT involved the atomic states $|2\rangle$, $|3\rangle$, and $|4\rangle$.

(ii) The two types of optical lattice patterns shown in Figs. 6(c) and 6(f) can be converted to each other through adjustments of $\rho_{22}^{(0)}/\rho_{11}^{(0)}$ and α_{12}/α_{11}.

(iii) When the $\rho_{22}^{(0)}/\rho_{11}^{(0)}$ is close to 1, i.e., the initial populations in two ground states are approximately equal (e.g., $\rho_{22}^{(0)}/\rho_{11}^{(0)} > 0.8$), the optical patterns are similar to those found in Figs. 5(b)–5(e), which are relevant to the domains 3–6 of Fig. 6(g) (not shown here to save space).

In addition, an optical phase separation can occur for large α_{12}/α_{11}, as indicated by the white color domain on the top of Fig. 6(g), which will be discussed in detail in the following section.

E. Optical phase separations and their control

We now investigate the optical phase separation in the system mentioned in the last three subsections in detail. Phase separation is a ubiquitous phenomenon in nature [51–60], which refers to a state of the system where two or more phases occur in different parts of the system, and the most common type of phase separation is between two immiscible fluids such as oil and water. We have shown that a similar phenomenon may appear in the present Rydberg atomic system, as illustrated in Figs. 4(f) and 5(f), where the distributions of two polarization components of the probe field appear separately in space.

The physical reason for the appearance of such an optical phase separation can be understood as follows. In many aspects, the motion of a light field behaves like that of a fluid flow [61]. In our system, the probe field has two components, which is similar to a mixture of two fluids. Since the interaction between Rydberg atoms under our study is repulsive, the system behaves like a two-fluid mixture, and the two components of the probe field will be immiscible if the cross-Kerr nonlinearities (denoted by the nonlinearity parameter α_{12}, which controls the mutual-interaction between the two components) reach a critical value.

From the phase diagrams shown in panel (g) of Figs. 4–6, we see that optical phase separations occur principally for the case of $\alpha_{12} > \alpha_{11}$. This is easy to understand because to realize the phase separations, the mutual-interaction between the two probe components (characterized by the cross-Kerr nonlinearities) must be larger than the self-interaction

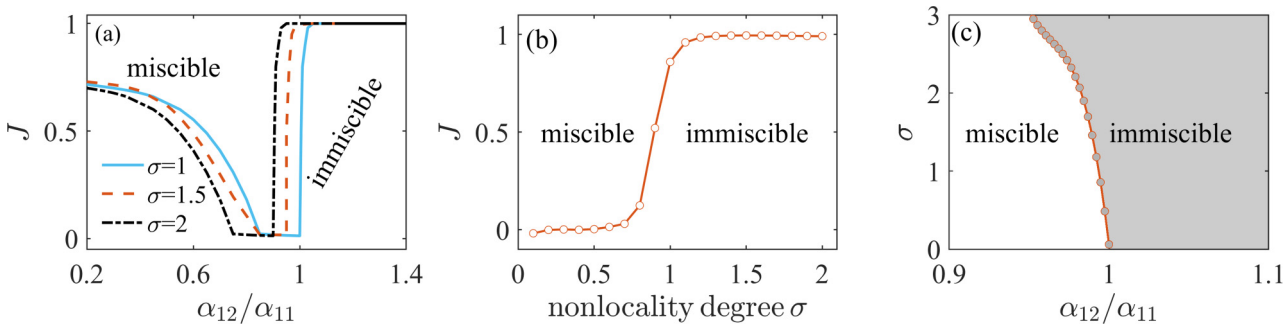

FIG. 7. Separation degree describing the optical phase separation and the phase diagram describing the transition from miscible to immiscible states. (a) Separation degree J as a function of the ratio of nonlinearity α_{12}/α_{11} (with $\alpha_{11} = 500$) and nonlocality degree of the Kerr nonlinearities σ. The solid blue, dashed red, and dotted black lines are for $\sigma = 1$, 1.5, and 2, respectively. (b) The circled solid red line is the separation degree J as a function of σ (with $\alpha_{11} = 500$ and $\alpha_{12}/\alpha_{11} = 0.95$). (c) Phase diagram describing the transition from miscible to immiscible states in the parameter plane $(\alpha_{12}/\alpha_{11}, \sigma)$. The circled solid red line is the boundary of the transition; the gray domain is relevant to Figs. 4(f) and 5(f) where optical phase separations occur.

(characterized by the self-Kerr nonlinearities) in the two probe components.

To quantify the optical phase separations in the system, we define the *separation degree*

$$J = 1 - \frac{\int |v_1(\vec{\zeta})||v_2(\vec{\zeta})|d^2\zeta}{[\int |v_1(\vec{\zeta})|^2 d^2\zeta \times \int |v_2(\vec{\zeta})|^2 d^2\zeta]^{1/2}}. \tag{13}$$

$J = 0$ ($J = 1$) describes a complete spatial overlap–miscibility (complete spatial separation–immiscibility) of the two components of the probe field. If $0 < J < 1$, the two components have a mixture in space, with the degree of the separation determined by the value of J. For example, in panels (d), (e), and (f) of Fig. 5, the values of J are 0.37, 0, and 1, respectively. When J has an intermediate value between 0 and 1 [e.g., Fig. 5(d) for which $J = 0.37$], the intensity distributions of both polarization components are full of whole space, with the bright spots locating in different positions. This is different from the case for $J = 1$ [i.e. Fig. 5(f)], where the distributions of the two polarization components are completely separated in space.

Shown in Fig. 7(a) is the separation degree J as a function of the ratio of nonlinearity α_{12}/α_{11} (with $\alpha_{11} = 500$ fixed) for different nonlocality degree of the Kerr nonlinearities σ. The solid blue, dashed red, and dotted black lines in the figure are for $\sigma = 1$, 1.5, and 2, respectively. We see that the two probe components are miscible (i.e. $J < 1$) for smaller α_{12}/α_{11} but immiscible (i.e., $J = 1$) for larger α_{12}/α_{11}, agreeing with the analysis given above and the results obtained in Figs. 4(a)–4(c) and Figs. 5(a)–5(c).

The circled solid red line in Fig. 7(b) is the separation degree J as a function of nonlocality degree σ (with $\alpha_{11} = 500$ and $\alpha_{12}/\alpha_{11} = 0.95$ fixed). One sees that the two probe components are miscible when the nonlocality degree σ is small, but they are immiscible when σ is large. This shows that the nonlocality degree of the Kerr nonlinearities can be used to manipulate the optical phase separation in the system.

To find a criterion for the transition between the miscible and immiscible states, following Refs. [53,56,60], the expression of the energy difference between the miscible and immiscible states of the system can be derived, given by

$$\Delta E = \frac{I_1 I_2}{V_{\rm tot}}\Big[\int \frac{1}{2}[\Re_{12}(\vec{\zeta}) + \Re_{21}(\vec{\zeta})]d^2\zeta - \Big(\int \Re_{11}(\vec{\zeta})d^2\zeta \times \int \Re_{22}(\vec{\zeta})d^2\zeta\Big)^{1/2}\Big], \tag{14}$$

with the derivation presented in Appendix E. Here $V_{\rm tot} = V_1 + V_2$, with V_1 and V_2 the volumes occupied by the v_1- and v_2-components, respectively. If $\Delta E > 0$ ($\Delta E < 0$), i.e., if the arithmetic mean of the nonlocal response functions for the cross-Kerr nonlinearities $\Re_{12}$ and $\Re_{21}$ is larger (smaller) than the geometric mean of the response functions of the self-Kerr nonlinearities $\Re_{11}$ and $\Re_{22}$, the system will have higher (lower) energy and hence will tend to go into an immiscible (miscible) state. The case $\Delta E = 0$ defines the critical value (boundary) for the transition from a miscible to an immiscible state [62].

Plotted in Fig. 7(c) is the result on the phase diagram describing the transition from the miscible to the immiscible state in the parameter plane $(\alpha_{12}/\alpha_{11}, \sigma)$ by using the criterion (14). The circled solid red line in the figure is the boundary for the transition; the gray domain corresponds to Figs. 4(f) and 5(f), where optical phase separations occur. We see that the domain for the optical immiscibility can be enlarged by increasing the nonlocality degree of the Kerr nonlinearities σ, which can be realized in the Rydberg atomic gas since the long-ranged Rydberg-Rydberg interaction plays an important role in such a system.

F. Nonlocal two-component optical solitons and vortices

In all of the considerations given above, the system is assumed to work in regimes where the four nonlocal response functions $\Re_{jl}$ ($j, l = 1, 2$) in Eqs. (7) are negative, based on which various optical patterns are obtained. Since the Rydberg atomic gas under consideration can be actively manipulated, one can choose different parameters to make the signs of $\Re_{jl}$ change, and hence it is possible to generate nonlocal two-component spatial solitons and vortices in the system. For example, all four response functions can be made to be positive if the system parameters are chosen to be $\Delta_2 = -2\pi \times$

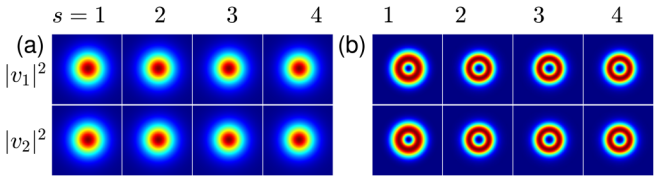

FIG. 8. Formation of the nonlocal spatial optical soliton and vortex pairs. (a) Spatial distributions of the bright-bright soliton pair for $s = z/(2L_{\rm diff}) = 1,\ 2,\ 3,\ 4$ by taking $|v_1|^2$ and $|v_2|^2$ as functions of $\xi = x/R_0$ and $\eta = y/R_0$ for $\sigma = 1$. (b) Spatial distributions of the vortex-vortex pair for $s = 1,\ 2,\ 3,\ 4$ for $\sigma = 1.8$.

0.4 MHz, $\Delta_3 = -2\pi \times 3.0$ MHz, $\Delta_4 = -2\pi \times 250$ MHz, $\Gamma_{12} = \Gamma_{21} = 2\pi \times 6$ MHz, $\Gamma_3 = \Gamma_4 = 2\pi \times 16.7$ kHz, $\Omega_c = 2\pi \times 25$ MHz, and $\mathcal{N}_a = 2.0 \times 10^{11}$ cm^{-3}. In this situation, the interaction between the two probe components becomes attractive; a plane-wave state may undergo a MI, which does not result in the formation of (extended) optical patterns but (localized) bright-bright soliton pairs.

Figure 8(a) shows the spatial distributions of a bright-bright soliton pair when it propagates, respectively, to the positions $s = z/(2L_{\rm diff}) = 1,\ 2,\ 3,\ 4$ by taking $|v_1|^2$ (top row) and $|v_2|^2$ (bottom row) as functions of $\xi = x/R_0$ and $\eta = y/R_0$ for $\sigma = 1$ (which gives $L_{\rm diff} = 0.94$ mm). The result is obtained by numerically solving Eqs. (7) based on the above parameters and with the initial condition $v_1 = v_2 = 2\,\mathrm{sech}(\sqrt{\xi^2+\eta^2}/2)$. We see that the soliton pair is quite stable during propagation.

Illustrated in Fig. 8(b) are the spatial distributions of a vortex-vortex pair when propagating, respectively, to the positions $s = z/(2L_{\rm diff}) = 1,\ 2,\ 3,\ 4$ for $\sigma = 1.8$ (which gives $L_{\rm diff} = 0.29$ mm). The result is obtained also by numerically solving Eqs. (7) with the initial condition $v_1 = v_2 = 2.3\,\zeta\, L_0^1(-\frac{\xi^2+\eta^2}{2})\exp(-\frac{\xi^2+\eta^2}{4})e^{i\phi}$. Here L_p^m is a generalized Laguerre polynomial, with (p, m) the mode indexes [63]; $\phi = \arctan(\eta/\xi)$ is a phase. One sees that the vortex-vortex pair is also quite stable during propagation.

If other system parameters are suitably chosen, one can realize the condition $\Re_{11} < 0$, $\Re_{12} < 0$, $\Re_{21} > 0$, and $\Re_{22} > 0$. In this case, the system supports stable bright-dark soliton pairs. The reason for the stability for both the 3D soliton-soliton and vortex-vortex pairs described above is that the Kerr nonlinearities in the Rydberg gas are nonlocal.

IV. DISCUSSION AND SUMMARY

The predictions of the stationary optical patterns and related structural phase transitions presented above may be observed experimentally by using a cold Rydberg atomic gas with the inverted Y-shaped level configuration. Since these lattice patterns form in the transverse x-y plane and the typical lattice separation is around 7 μm, one should prepare a Rydberg gas of transverse size of several tens of micrometers (e.g., 30 μm); furthermore, to form a clear optical pattern based on the MI starting from a plane-wave probe field plus a random initial condition, the longitudinal size of the gas should be larger than the nonlinearity length $L_{\rm non}$ and the diffraction length $L_{\rm diff}$; both of them are around 0.2 mm [see Figs. 1(c1)–1(c3)], which can be realized by current experimental techniques [64]. Comparably, the observation of the spatial optical solitons and vortices needs flexible conditions, for which the transverse size of 10 micrometers is enough because the typical transverse size of the solitons and vortices is only several micrometers. To realize the predicted optical structures, one can inject a continuous-wave probe beam with two orthogonally polarized components; under the condition of the double EIT and by setting suitable system parameters, the probe beam will undergo MI and then be transformed into the spatial optical patterns, solitons, and vortices along the z-direction for several millimeters.

In the present work, as in Ref. [18], we have limited our considerations only for stationary optical structures based on the assumption that the probe field is a CW spatial light beam; the spatial optical structures are obtained by using an "imaginary-time" propagation method [i.e., $z \to iz$ in Eq. (5)], by which the ground-state solutions can be acquired very quickly for a short propagation distance. A canonical approach for the optical pattern formation relevant to experimental observation would be to propagate the light fields through the medium along the z direction and look at the transverse patterns after some propagation distance by using a real-time propagation method [which has been used only for Fig. 1(c) in our work]. It is available to get temporally oscillatory optical structures in the system through Hopf bifurcations by considering the case beyond the CW approximation, so that the eigenvalues of the eigenequations in MI analysis may have both real and imaginary parts (such as those described in Refs. [65–67]), an interesting topic that deserves to be explored further.

In conclusion, we have investigated the formation and control of spatial optical patterns in a cold Rydberg atomic gas via double Rydberg-EIT. Based on the analysis on the coupled 3D NNLS equations derived from the MB equations, we found that through the MI of the homogeneous plane-wave state of the two-component probe field, the system undergoes a spontaneous symmetry breaking and hence the emergence of various self-organized optical lattice structures, which can be controlled by the ratio between the cross- and self-Kerr nonlinearities, the nonlocality degree of the Kerr nonlinearities, and the populations initially prepared in the two atomic ground states. In particular, a crossover from phase mixture to phase separation of the two components of the probe field may appear when the ratio between the cross- and self-Kerr nonlinearities passes over a critical value. We also found that the system supports a nonlocal two-component spatial optical soliton and vortices when the parameters of the system are selected suitably. The results obtained in this work are not only useful for obtaining novel optical structures and realizing their active manipulations, but they are also promising for practical applications, e.g., for the design of nonlinear optical splitters based on the optical phase separation reported here.

ACKNOWLEDGMENTS

This work was supported by the National Natural Science Foundation of China under Grant No. 11975098 and the Research Funds of Happiness Flower ECNU under Grant No. 2020ECNU-XFZH005.

APPENDIX A: OPTICAL BLOCH EQUATION AND ITS SOLUTIONS

1. Optical Bloch equation

The explicit expression of the optical Bloch equation (2) is given by [68]

$$i\frac{\partial\rho_{11}}{\partial t}+i\Gamma_{21}\rho_{11}-i\Gamma_{12}\rho_{22}-i\Gamma_{13}\rho_{33}+\Omega_{p1}^{*}\rho_{31}-\Omega_{p1}\rho_{13}=0, \tag{A1a}$$

$$i\frac{\partial\rho_{22}}{\partial t}-i\Gamma_{21}\rho_{11}+i\Gamma_{12}\rho_{22}-i\Gamma_{23}\rho_{33}+\Omega_{p2}^{*}\rho_{32}-\Omega_{p2}\rho_{23}=0, \tag{A1b}$$

$$i\frac{\partial\rho_{33}}{\partial t}-i\Gamma_{34}\rho_{44}+i\Gamma_{3}\rho_{33}+(\Omega_{p1}\rho_{13}+\Omega_{p2}\rho_{23}+\Omega_{c}^{*}\rho_{43}-\text{c.c.})=0, \tag{A1c}$$

$$i\frac{\partial\rho_{44}}{\partial t}+i\Gamma_{34}\rho_{44}-\Omega_{c}^{*}\rho_{43}+\Omega_{c}\rho_{34}=0 \tag{A1d}$$

for diagonal elements, and

$$\left(i\frac{\partial}{\partial t}+d_{21}\right)\rho_{21}+\Omega_{p2}^{*}\rho_{31}-\Omega_{p1}\rho_{23}=0, \tag{A2a}$$

$$\left(i\frac{\partial}{\partial t}+d_{31}\right)\rho_{31}+\Omega_{c}^{*}\rho_{41}+\Omega_{p1}(\rho_{11}-\rho_{33})+\Omega_{p2}\rho_{21}=0, \tag{A2b}$$

$$\left(i\frac{\partial}{\partial t}+d_{32}\right)\rho_{32}+\Omega_{c}^{*}\rho_{42}+\Omega_{p1}\rho_{12}+\Omega_{p2}(\rho_{22}-\rho_{33})=0, \tag{A2c}$$

$$\left(i\frac{\partial}{\partial t}+d_{41}\right)\rho_{41}+\Omega_{c}\rho_{31}-\Omega_{p1}\rho_{43}-\frac{1}{2}\mathcal{N}_{a}\int d^{3}r'\mathcal{V}(\mathbf{r}'-\mathbf{r})\rho_{44,41}(\mathbf{r}',\mathbf{r},t)=0, \tag{A2d}$$

$$\left(i\frac{\partial}{\partial t}+d_{42}\right)\rho_{42}+\Omega_{c}\rho_{32}-\Omega_{p2}\rho_{43}-\frac{1}{2}\mathcal{N}_{a}\int d^{3}r'\mathcal{V}(\mathbf{r}'-\mathbf{r})\rho_{44,42}(\mathbf{r}',\mathbf{r},t)=0, \tag{A2e}$$

$$\left(i\frac{\partial}{\partial t}+d_{43}\right)\rho_{43}-\Omega_{p1}^{*}\rho_{41}-\Omega_{p2}^{*}\rho_{42}+\Omega_{c}(\rho_{33}-\rho_{44})-\frac{1}{2}\mathcal{N}_{a}\int d^{3}r'\mathcal{V}(\mathbf{r}'-\mathbf{r})\rho_{44,43}(\mathbf{r}',\mathbf{r},t)=0 \tag{A2f}$$

for nondiagonal elements. Here $d^3r'=dx'dy'dz'$; $d_{\alpha\beta}=\Delta_\alpha-\Delta_\beta+i\gamma_{\alpha\beta}$ ($\alpha,\beta=1,2,3,4;\alpha\neq\beta$); $\Delta_1=0$, $\Delta_2=\omega_1-\omega_2$, $\Delta_3=\omega_p-(\omega_3-\omega_1)$, and $\Delta_4=\omega_c+\omega_p-(\omega_4-\omega_1)$ are, respectively, one- and two-photon detunings; $\gamma_{\alpha\beta}=(\Gamma_\alpha+\Gamma_\beta)/2+\gamma_{\alpha\beta}^{\text{dep}}$ with $\Gamma_\alpha=\sum_{\alpha<\beta}\Gamma_{\alpha\beta}$ ($\Gamma_{\alpha\beta}$ and $\gamma_{\alpha\beta}^{\text{dep}}$ are the spontaneous emission decay rate and dephasing rate from $|\beta\rangle$ to $|\alpha\rangle$, respectively).

Although Eq. (2) describes the evolution of the matrix elements $\rho_{\alpha\beta}(\mathbf{r},t)$ of the one-body reduced DM $\rho(\mathbf{r},t)$, they involve two-body reduced DM $\rho_{\text{twobody}}(\mathbf{r}',\mathbf{r},\mathbf{t})$ with matrix elements defined by $\rho_{\alpha\beta,\mu\nu}(\mathbf{r}',\mathbf{r},t)=\langle\hat{S}_{\alpha\beta}(\mathbf{r}',t)\hat{S}_{\mu\nu}(\mathbf{r},t)\rangle$ (or called two-body correlators) due to the Rydberg-Rydberg interaction. So Eq. (2) is not a closed one, and one must solve the equations for the two-body DM elements. For example, the equation of two-body matrix element $\rho_{44,41}\equiv\langle\hat{S}_{44}(\mathbf{r}',t)\hat{S}_{41}(\mathbf{r},t)\rangle$ reads

$$\left[i\frac{\partial}{\partial t}+d_{41}+i\Gamma_{34}-\mathcal{V}(\mathbf{r}'-\mathbf{r})\right]\rho_{44,41}-\Omega_{c}^{*}\rho_{43,41}+\Omega_{c}(\rho_{34,41}+\rho_{44,31})-\Omega_{p1}\rho_{44,43}$$
$$-\frac{\mathcal{N}_{a}}{2}\int d^{3}r''\mathcal{V}(\mathbf{r}''-\mathbf{r})\rho_{44,44,41}(\mathbf{r}'',\mathbf{r}',\mathbf{r},t)=0. \tag{A3}$$

We see that it involves three-body DM element $\rho_{44,44,41}(\mathbf{r}'',\mathbf{r}',\mathbf{r},t)\equiv\langle\hat{S}_{44}(\mathbf{r}'',t)\hat{S}_{44}(\mathbf{r}',t)\hat{S}_{41}(\mathbf{r},t)\rangle$. The equations for other two-body DM elements are too lengthy and hence are omitted here to save space. Thus, to solve the equations of the one-body and two-body DM elements above, we need the equations of three-body DM elements. In a similar way, we can get the equations of motion for the three-body DM elements, which, however, involve four-body DM elements (omitted here), and so on. To solve such a chain of infinite equations for N-body ($N=1,2,3,\dots$) DM elements, a suitable truncation technique beyond the mean-field approximation is needed, which has been developed recently [12,14,41]. Based on such an approach, we can solve the MB equations (2) and (3) by using an asymptotic expansion in a consistent and standard way.

2. Equations of motion of density-matrix elements and their solutions up to third-order approximations

We are interested in stationary states of the system, and hence the time derivatives in the MB equations (2) can be neglected (i.e., $\partial/\partial t=0$), which is valid if the probe and control fields have a large time duration. We adopt the method developed in Refs. [12,14,41] to first solve the Bloch equation (2) under the condition of Rydberg-EIT. We assume that all the atoms are initially prepared in the ground states $|1\rangle$ and $|2\rangle$.

Since the probe field is weak, we can take $\Omega_{pj} \sim \epsilon$ as an expansion parameter, and make the expansion $\rho_{\alpha\beta} = \epsilon\rho^{(1)}_{\alpha\beta} + \epsilon^2\rho^{(2)}_{\alpha\beta} + \cdots$ $(\beta = 1, 2; \alpha = 2, 3, 4; \beta < \alpha)$. Substituting the expansions into Eq. (2), and collecting coefficients of ϵ^l $(l = 0, 1, 2, \ldots)$, we obtain a series of linear but inhomogeneous equations that can be solved order by order:

(i) First-order solution: At the first order $(l = 1)$, we obtain

$$\rho^{(1)}_{ij} = [\delta_{i3}d_{4j} - \delta_{i4}\Omega_c]\rho^{(0)}_{jj}\Omega_{pj}/D_j \tag{A4}$$

for $i = 3, 4$ and $j = 1, 2$ (other $\rho^{(1)}_{\alpha\beta}$ are zero), with $D_j = |\Omega_c|^2 - d_{3j}d_{4j}$.

(ii) Second-order solution: Solving the second-order $(l = 2)$ equations yields

$$\rho^{(2)}_{21} = a^{(2)}_{21}\Omega_{p1}\Omega^*_{p2}, \tag{A5a}$$

$$\rho^{(2)}_{\alpha\alpha} = a^{(2)}_{\alpha\alpha,1}|\Omega_{p1}|^2 + a^{(2)}_{\alpha\alpha,2}|\Omega_{p2}|^2 \ (\alpha = 1 - 4), \tag{A5b}$$

$$\rho^{(2)}_{43} = a^{(2)}_{43,1}|\Omega_{p1}|^2 + a^{(2)}_{43,2}|\Omega_{p2}|^2, \tag{A5c}$$

in which

$$\begin{aligned}
a^{(2)}_{33,j} &= \rho^{(0)}_{jj}N_j/(i\Gamma_3),\\
a^{(2)}_{21} &= \big(\rho^{(0)}_{22}d^*_{42}/D^*_2 - \rho^{(0)}_{11}d_{41}/D_1\big)/d_{21},\\
a^{(2)}_{44,j} &= \rho^{(0)}_{jj}|\Omega_c|^2\big[M_j + N_jM_3/(i\Gamma_3)\big]/(i\Gamma_{34} + M_3|\Omega_c|^2),\\
a^{(2)}_{22,j} &= -\big[(\Gamma_{13} + \Gamma_{21})a^{(2)}_{33,j} + \Gamma_{21}a^{(2)}_{44,j} + \delta_{1j}iN_1\rho^{(0)}_{11}\big]/\Gamma_2,\\
a^{(2)}_{43,j} &= -\Omega_c\big[\rho^{(0)}_{jj}/D_j + a^{(2)}_{33,j} - a^{(2)}_{44,j}\big]/d_{43},\\
a^{(2)}_{11,j} &= -\big(a^{(2)}_{22,j} + a^{(2)}_{33,j} + a^{(2)}_{44,j}\big).
\end{aligned}$$

Here $N_j = 2i\,\mathrm{Im}(d_{4j}/D_j)$, $M_j = 2i\,\mathrm{Im}[1/(D^*_jd^*_{43})]$, $M_3 = 2i\,\mathrm{Im}(1/d^*_{43})$, $\Gamma_2 = \Gamma_{12} + \Gamma_{21}$, and $\Gamma_3 = \Gamma_{13} + \Gamma_{23}$ $(j = 1, 2)$.

(iii) Third-order solution: The solutions of $\rho^{(3)}_{\alpha1}$ and $\rho^{(3)}_{\alpha2}$ $(\alpha = 3, 4)$ are given by

$$\rho^{(3)}_{\alpha1} = \big[a^{(3)}_{\alpha1,1}|\Omega_{p1}|^2 + a^{(3)}_{\alpha1,2}|\Omega_{p2}|^2\big]\Omega_{p1} + \mathcal{N}_a\Omega^*_c/D_1\int d^3r'\mathcal{V}(\mathbf{r}' - \mathbf{r})\big[a^{(3)}_{44,41,1}|\Omega_{p1}|^2 + a^{(3)}_{44,41,2}|\Omega_{p2}|^2\big]\Omega_{p1}, \tag{A6a}$$

$$\rho^{(3)}_{\alpha2} = \big[a^{(3)}_{\alpha2,1}|\Omega_{p1}|^2 + a^{(3)}_{\alpha2,2}|\Omega_{p2}|^2\big]\Omega_{p2} + \mathcal{N}_a\Omega^*_c/D_2\int d^3r'\mathcal{V}(\mathbf{r}' - \mathbf{r})\big[a^{(3)}_{44,42,1}|\Omega_{p1}|^2 + a^{(3)}_{44,42,2}|\Omega_{p2}|^2\big]\Omega_{p2}, \tag{A6b}$$

in which

$$\begin{aligned}
a^{(3)}_{31,j} &= \big[\Omega^*_ca^{(2)}_{43,j} + d_{41}\big(a^{(2)}_{11,j} - a^{(2)}_{33,j}\big) + \delta_{2j}a^{(2)}_{21}d_{41}\big]/D_1,\\
a^{(3)}_{32,j} &= \big[\Omega^*_ca^{(2)}_{43,j} + d_{42}\big(a^{(2)}_{22,j} - a^{(2)}_{33,j}\big) + \delta_{1j}a^{*(2)}_{21}d_{42}\big]/D_2,\\
a^{(3)}_{41,j} &= \big[\Omega_c\big(a^{(2)}_{33,j} - a^{(2)}_{11,j}\big) - d_{31}a^{(2)}_{43,j} - \delta_{2j}\Omega_ca^{(2)}_{21}\big]/D_1,\\
a^{(3)}_{42,j} &= \big[\Omega_c\big(a^{(2)}_{33,j} - a^{(2)}_{22,j}\big) - d_{32}a^{(2)}_{43,j} - \delta_{1j}\Omega_ca^{*(2)}_{21}\big]/D_2,
\end{aligned}$$

where the coefficients of two-body DM elements $a^{(3)}_{44,4j,\alpha} = a^{(3)}_{44,4j,\alpha}(\mathbf{r}', \mathbf{r}, t)$ $(j = 1, 2; \alpha = 1, 2)$ are functions of $\mathbf{r}'$, $\mathbf{r}$, and t, yet to be determined (see below).

(iv) Second-order solution for two-body DM elements: Notice that for obtaining the solution of $\rho^{(3)}_{\alpha\beta}$ $(\alpha = 3, 4; \beta = 1, 2)$, equations for some two-body DM elements $\rho_{\alpha\beta,\mu\nu}$ must be solved simultaneously. These two-body DM elements are nonzero starting at ϵ^2-order, so they can be assumed to have the form $\rho_{\alpha\beta,\mu\nu} = \epsilon^2\rho^{(2)}_{\alpha\beta,\mu\nu} + \epsilon^3\rho^{(3)}_{\alpha\beta,\mu\nu} + \cdots$. Then we have the equations for the second-order two-body DM elements $\rho^{(2)}_{\alpha j,\beta j}$ $(\alpha, \beta = 3, 4;\ j = 1, 2)$:

$$\begin{pmatrix} d_{3j} & \Omega^*_c & 0\\ \Omega_c & d_{3j} + d_{4j} & \Omega^*_c\\ 0 & 2\Omega_c & A\end{pmatrix}\begin{pmatrix}\rho^{(2)}_{3j,3j}\\ \rho^{(2)}_{4j,3j}\\ \rho^{(2)}_{4j,4j}\end{pmatrix} = -\begin{pmatrix}a^{(1)}_{3j}\\ a^{(1)}_{4j}\\ 0\end{pmatrix}\rho^{(0)}_{jj}\Omega^2_{pj}, \tag{A7}$$

$$\begin{pmatrix} B & \Omega_c & \Omega_c & 0\\ \Omega^*_c & d_{41} + d_{32} & 0 & \Omega_c\\ \Omega^*_c & 0 & d_{42} + d_{31} & \Omega_c\\ 0 & \Omega^*_c & \Omega^*_c & d_{32} + d_{31}\end{pmatrix}\begin{pmatrix}\rho^{(2)}_{42,41}\\ \rho^{(2)}_{41,32}\\ \rho^{(2)}_{42,31}\\ \rho^{(2)}_{32,31}\end{pmatrix} = -\begin{pmatrix}0\\ a^{(1)}_{41}\rho^{(0)}_{22}\\ a^{(1)}_{42}\rho^{(0)}_{11}\\ a^{(1)}_{32}\rho^{(0)}_{11} + a^{(1)}_{31}\rho^{(0)}_{22}\end{pmatrix}\Omega_{p1}\Omega_{p2}, \tag{A8}$$

with $A = 2d_{4j} - \frac{1}{2}\mathcal{V}(\mathbf{r})$ and $B = d_{41} + d_{42} - \frac{1}{2}\mathcal{V}(\mathbf{r})$. We obtain $\rho^{(2)}_{\alpha j,\beta j} = Q_{0j}/[P_{0j} + P_{1j}\mathcal{V}(\mathbf{r})]$, where P_{0j}, P_{1j}, Q_{0j} are functions of the detunings, spontaneous emission decay rate, and dephasing rates of the system (their explicit expressions are omitted here).

(v) Third-order solution for two-body DM elements: The third-order solution of the two-body DM elements satisfies the equation

$$\mathbf{M}\cdot\rho = \mathbf{C}_1|\Omega_{p2}|^2\Omega_{p1} + \mathbf{C}_2|\Omega_{p1}|^2\Omega_{p1}, \tag{A9}$$

where

$$\mathbf{M} = \begin{pmatrix} m_1 & -\Omega_c^* & \Omega_c & \Omega_c & 0 & 0 & 0 & 0 \\ -\Omega_c & m_2 & 0 & 0 & \Omega_c & \Omega_c & 0 & 0 \\ -\Omega_c^* & 0 & m_3 & 0 & \Omega_c^* & 0 & -\Omega_c & 0 \\ \Omega_c^* & 0 & 0 & m_4 & 0 & -\Omega_c^* & \Omega_c & 0 \\ -i\Gamma_{34} & \Omega_c^* & -\Omega_c & 0 & m_5 & 0 & 0 & \Omega_c \\ 0 & \Omega_c^* & 0 & -\Omega_c & 0 & m_6 & 0 & \Omega_c \\ 0 & 0 & -\Omega_c^* & -\Omega_c^* & 0 & 0 & m_7 & \Omega_c^* \\ 0 & 0 & 0 & -i\Gamma_{34} & \Omega_c^* & \Omega_c^* & -\Omega_c & m_8 \end{pmatrix},$$

$$\mathbf{C}_1 = \left[0, a^{(2)}_{42,41}, a^{*(2)}_{42,14}, -a^{(2)}_{44,2}\rho^{(0)}_{11}, a^{(2)}_{41,32} - a^{(2)}_{41,23}, a^{(2)}_{42,31} - a^{(2)}_{43,2}\rho^{(0)}_{11}, a^{*(2)}_{42,13} + a^{*(2)}_{43,2}\rho^{(0)}_{11}, a^{(2)}_{32,31} - a^{(2)}_{33,2}\rho^{(0)}_{11} - a^{*(2)}_{32,13}\right]^T,$$

$$\mathbf{C}_2 = \left[0, a^{(2)}_{41,41}, a^{*(2)}_{41,14}, -a^{(2)}_{44,1}\rho^{(0)}_{11}, a^{(2)}_{41,31} - a^{(2)}_{41,13}, a^{(2)}_{41,31} - a^{(2)}_{43,1}\rho^{(0)}_{11}, a^{*(2)}_{41,13} + a^{*(2)}_{43,1}\rho^{(0)}_{11}, a^{(2)}_{31,31} - a^{(2)}_{31,13} - a^{(2)}_{33,1}\rho^{(0)}_{11}\right]^T,$$

$$\rho = \left[\rho^{(3)}_{44,41}, \rho^{(3)}_{43,41}, \rho^{*(3)}_{43,14}, \rho^{(3)}_{44,31}, \rho^{(3)}_{41,33}, \rho^{(3)}_{43,31}, \rho^{*(3)}_{43,13}, \rho^{(3)}_{33,31}\right]^T,$$

with $m_1 = i\Gamma_{34} + d_{41} - \frac{1}{2}\mathcal{V}$, $m_2 = d_{43} + d_{41} - \frac{1}{2}\mathcal{V}$, $m_3 = d^*_{43} + d^*_{14}$, $m_4 = i\Gamma_{34} + d_{31}$, $m_5 = d_{41} + i\Gamma_3$, $m_6 = d_{43} + d_{31}$, $m_7 = d^*_{43} + d^*_{13}$, and $m_8 = i\Gamma_3 + d_{31}$.

The equation for $\rho\rho^{(3)}_{44,42}$ reads

$$\mathbf{N}\cdot\rho = \mathbf{C}_3|\Omega_{p2}|^2\Omega_{p2} + \mathbf{C}_4|\Omega_{p1}|^2\Omega_{p2}, \tag{A10}$$

where

$$\mathbf{N} = \begin{pmatrix} n_1 & -\Omega_c^* & \Omega_c & \Omega_c & 0 & 0 & 0 & 0 \\ -\Omega_c & n_2 & 0 & 0 & \Omega_c & \Omega_c & 0 & 0 \\ -\Omega_c^* & 0 & n_3 & 0 & 0 & \Omega_c^* & -\Omega_c & 0 \\ \Omega_c^* & 0 & 0 & n_4 & -\Omega_c^* & 0 & \Omega_c & 0 \\ 0 & \Omega_c^* & 0 & -\Omega_c & n_5 & 0 & 0 & \Omega_c \\ -i\Gamma_{34} & \Omega_c^* & -\Omega_c & 0 & 0 & n_6 & 0 & \Omega_c \\ 0 & 0 & -\Omega_c^* & -\Omega_c^* & 0 & 0 & n_7 & \Omega_c^* \\ 0 & 0 & 0 & -i\Gamma_{34} & \Omega_c^* & \Omega_c^* & -\Omega_c & n_8 \end{pmatrix},$$

$$\mathbf{C}_3 = \left[0, a^{(2)}_{42,42}, a^{(2)}_{42,24}, -a^{(2)}_{44,2}\rho^{(0)}_{22}, a^{(2)}_{42,32} - a^{(2)}_{43,2}\rho^{(0)}_{22}, a^{(2)}_{42,32} - a^{(2)}_{42,23}, a^{*(2)}_{42,23} + a^{*(2)}_{43,2}\rho^{(0)}_{22}, a^{(2)}_{32,32} - a^{(2)}_{32,23} - a^{(2)}_{33,2}\rho^{(0)}_{22}\right]^T,$$

$$\mathbf{C}_4 = \left[0, a^{(2)}_{42,41}, a^{(2)}_{42,14}, -a^{(2)}_{44,1}, a^{(2)}_{41,32} - a^{(2)}_{43,1}, a^{(2)}_{42,31} - a^{(2)}_{42,13}, a^{*(2)}_{41,23} + a^{*(2)}_{43,1}\rho^{(0)}_{22}, a^{(2)}_{32,31} - a^{(2)}_{32,13} - a^{(2)}_{33,1}\rho^{(0)}_{22}\right]^T$$

$$\rho = \left[\rho^{(3)}_{44,42}, \rho^{(3)}_{43,42}, \rho^{*(3)}_{43,24}, \rho^{(3)}_{44,32}, \rho^{(3)}_{43,32}, \rho^{(3)}_{42,33}, \rho^{*(3)}_{43,23}, \rho^{(3)}_{33,32}\right],$$

with $n_1 = i\Gamma_{34} + d_{42} - \frac{1}{2}\mathcal{V}$, $n_2 = d_{43} + d_{42} - \frac{1}{2}\mathcal{V}$, $n_3 = d^*_{43} + d^*_{24}$, $n_4 = i\Gamma_{34} + d_{32}$, $n_5 = d_{43} + d_{32}$, $n_6 = d_{42} + i\Gamma_3$, $n_7 = d^*_{43} + d^*_{23}$, and $n_8 = i\Gamma_3 + d_{32}$.

By solving Eqs. (A9) and (A10), we obtain the solution $\rho^{(3)}_{44,4j}$ with the form

$$\rho^{(3)}_{44,41} = a^{(3)}_{44,41,1}|\Omega_{p1}|^2\Omega_{p1} + a^{(3)}_{44,41,2}|\Omega_{p2}|^2\Omega_{p1}, \tag{A11a}$$

$$\rho^{(3)}_{44,42} = a^{(3)}_{44,42,1}|\Omega_{p1}|^2\Omega_{p2} + a^{(3)}_{44,42,2}|\Omega_{p2}|^2\Omega_{p2}, \tag{A11b}$$

in which

$$a^{(3)}_{44,4j,l} = \frac{\sum_{m=0}^{2} P_{jlm}\mathcal{V}^m(\mathbf{r}' - \mathbf{r})}{\sum_{n=0}^{3} Q_{jln}\mathcal{V}^n(\mathbf{r}' - \mathbf{r})}. \tag{A12}$$

Here P_{jln} and Q_{jln} $(j, l = 1, 2)$ are constants, depending on the spontaneous emission and dephasing rates, detunings, half Rabi frequency of the control field, as well as other parameters of the system. Thereby, based on the first-, second-, and third-order solutions given above, one can obtain the explicit expression of the one-body DM elements up to third-order approximation, i.e., $\rho_{3j} \approx \rho^{(1)}_{3j} + \rho^{(2)}_{3j} + \rho^{(3)}_{3j}$ $(j = 1, 2)$.

APPENDIX B: EXPRESSIONS OF THE NONLINEAR OPTICAL SUSCEPTIBILITIES AND THE DERIVATION OF THE COUPLED NLSES

The optical susceptibility χ_j of the jth polarization component of the probe field is given by $\chi_j = \mathcal{N}_a(\hat{\mathbf{e}}_{p\pm}\cdot\mathbf{p}_{j3})\rho_{3j}/(\varepsilon_0\mathcal{E}_\pm)$ $(j=1,2)$, which has the form

$$\chi_j = \chi_j^{(1)} + \left[\chi_{j,\mathrm{loc}}^{(3,s)} + \chi_{j,\mathrm{nloc}}^{(3,s)}\right]|\mathcal{E}_{p\pm}|^2 + \left[\chi_{j,\mathrm{loc}}^{(3,c)} + \chi_{j,\mathrm{nloc}}^{(3,c)}\right]|\mathcal{E}_{p\mp}|^2, \tag{B1}$$

where

$$\chi_j^{(1)} = \mathcal{N}_a|p_{j3}|^2 d_{4j}\rho_{jj}^{(0)}/(\varepsilon_0\hbar D_j), \tag{B2a}$$

$$\chi_{j,\mathrm{loc}}^{(3,s)} = \mathcal{N}_a a_{3j,j}^{(3)}|p_{j3}|^4/(\varepsilon_0\hbar^3), \tag{B2b}$$

$$\chi_{j,\mathrm{loc}}^{(3,c)} = \mathcal{N}_a a_{3j,3-j}^{(3)}|p_{13}|^2|p_{23}|^2/(\varepsilon_0\hbar^3), \tag{B2c}$$

$$\chi_{j,\mathrm{nloc}}^{(3,s)} = \frac{\mathcal{N}_a^2\Omega_c^*}{2\varepsilon_0\hbar^3 D_j}\int d^3r'\mathcal{V}(\mathbf{r}'-\mathbf{r})a_{44,4j,j}^{(3)}(\mathbf{r}',\mathbf{r})|\mathbf{p}_{j3}|^4, \tag{B2d}$$

$$\chi_{j,\mathrm{nloc}}^{(3,c)} = \frac{\mathcal{N}_a^2\Omega_c^*}{2\varepsilon_0\hbar^3 D_j}\int d^3r'\mathcal{V}(\mathbf{r}'-\mathbf{r})a_{44,4j,3-j}^{(3)}(\mathbf{r}',\mathbf{r})|\mathbf{p}_{13}|^2|\mathbf{p}_{23}|^2. \tag{B2e}$$

Substituting the results of ρ_{31} and ρ_{32} [Eqs. (A6) and (A11)] into Maxwell Eq. (3), we obtain the envelope equations controlling the dynamics of the two polarization components of the probe field, which have the form of the coupled 3D NNLS equations

$$i\frac{\partial\Omega_{p1}}{\partial z} + \frac{c}{2\omega_p}\nabla_\perp^2\Omega_{p1} + (W_{11}|\Omega_{p1}|^2 + W_{12}|\Omega_{p2}|^2)\Omega_{p1} + \int d^3r'\mathcal{N}_{11}(\mathbf{r}'-\mathbf{r})|\Omega_{p1}(\mathbf{r}')|^2\Omega_{p1}(\mathbf{r}) + \int d^3r'\mathcal{N}_{12}(\mathbf{r}'-\mathbf{r})|\Omega_{p2}(\mathbf{r}')|^2\Omega_{p1}(\mathbf{r}) = 0, \tag{B3a}$$

$$i\frac{\partial\Omega_{p2}}{\partial z} + \frac{c}{2\omega_p}\nabla_\perp^2\Omega_{p2} + (W_{22}|\Omega_{p2}|^2 + W_{21}|\Omega_{p1}|^2)\Omega_{p2} + \int d^3r'\mathcal{N}_{22}(\mathbf{r}'-\mathbf{r})|\Omega_{p2}(\mathbf{r}')|^2\Omega_{p2}(\mathbf{r}) + \int d^3r'\mathcal{N}_{21}(\mathbf{r}'-\mathbf{r})|\Omega_{p1}(\mathbf{r}')|^2\Omega_{p2}(\mathbf{r}) = 0, \tag{B3b}$$

where

$$W_{1l} = \kappa_{13}\left[\Omega_c^* a_{43,l}^{(2)} + d_{41}(a_{11,l}^{(2)} - a_{33,l}^{(2)}) + \delta_{l2}a_{21}^{(2)}\right]/D_1, \tag{B4a}$$

$$W_{2l} = \kappa_{23}\left[\Omega_c^* a_{43,l}^{(2)} + d_{42}(a_{22,l}^{(2)} - a_{33,l}^{(2)}) + \delta_{l2}a_{21}^{*(2)}\right]/D_2, \tag{B4b}$$

$$\mathcal{N}_{jl} = \frac{1}{2}\kappa_{13}\Omega_c^*\mathcal{N}_a\mathcal{V}(\mathbf{r}'-\mathbf{r})a_{44,4j,l}^{(3)}(\mathbf{r}'-\mathbf{r})/D_j. \tag{B4c}$$

The coefficient W_{jl} $[\mathcal{N}_{jl}(\mathbf{r}'-\mathbf{r})]$ characterizes the local (nonlocal) self-Kerr $(j=l)$ and cross-Kerr $(j\neq l)$ nonlinearity of the jth polarization components of the probe field. For simplicity, we assume that the probe field is slowly varied along the z direction, so that a local approximation in this direction can be made for the nonlinear response function. Then Eqs. (B3) are reduced to

$$i\frac{\partial\Omega_{p1}}{\partial z} + \frac{c}{2\omega_p}\nabla_\perp^2\Omega_{p1} + (W_{11}|\Omega_{p1}|^2 + W_{12}|\Omega_{p2}|^2)\Omega_{p1} + \int d^2r'\left[\mathcal{N}_{11}'(\mathbf{r}_\perp'-\mathbf{r}_\perp)|\Omega_{p1}(\mathbf{r}_\perp',z)|^2 + \mathcal{N}_{12}'(\mathbf{r}_\perp'-\mathbf{r}_\perp)|\Omega_{p2}(\mathbf{r}_\perp',z)|^2\right]\Omega_{p1}(\mathbf{r}_\perp) = 0, \tag{B5a}$$

$$i\frac{\partial\Omega_{p2}}{\partial z} + \frac{c}{2\omega_p}\nabla_\perp^2\Omega_{p2} + (W_{22}|\Omega_{p2}|^2 + W_{21}|\Omega_{p1}|^2)\Omega_{p2} + \int d^2r_\perp'\left[\mathcal{N}_{22}'(\mathbf{r}_\perp'-\mathbf{r}_\perp)|\Omega_{p2}(\mathbf{r}_\perp',z)|^2 + \mathcal{N}_{21}'(\mathbf{r}_\perp'-\mathbf{r}_\perp)|\Omega_{p1}(\mathbf{r}_\perp',z)|^2\right]\Omega_{p2}(\mathbf{r}_\perp) = 0, \tag{B5b}$$

where $\mathbf{r}_\perp = (x,y)$ and $d^2r_\perp = dx'dy'$, and the reduced nonlocal nonlinear response function reads $\mathcal{N}_{jl}'(\mathbf{r}_\perp) = \int\mathcal{N}_{jl}(\mathbf{r})dz$. Equations (B5) can be cast into the dimensionless form

$$i\frac{\partial u_1}{\partial s} + \tilde{\nabla}_\perp^2 u_1 + (w_{11}|u_1|^2 + w_{12}|u_2|^2)u_1 + \int d^2\zeta'[\Re_{11}(\vec{\zeta}'-\vec{\zeta})|u_1(\vec{\zeta}')|^2 + \Re_{12}(\vec{\zeta}'-\vec{\zeta})|u_2(\vec{\zeta}')|^2]u_1 = 0, \tag{B6}$$

$$i\frac{\partial u_2}{\partial s} + \tilde{\nabla}_\perp^2 u_2 + (w_{22}|u_2|^2 + w_{21}|u_1|^2)u_2 + \int d^2\zeta'[\Re_{22}(\vec{\zeta}'-\vec{\zeta})|u_2(\vec{\zeta}')|^2 + \Re_{21}(\vec{\zeta}'-\vec{\zeta})|u_1(\vec{\zeta}')|^2]u_2 = 0, \tag{B7}$$

where $u_j = \Omega_{pj}/U_0$ (U_0 is the typical half Rabi frequency of the probe field), $s = z/(2L_{\rm diff})$ ($L_{\rm diff} = \omega_p R_0^2/c$ is the typical diffraction length; R_0 is the typical transverse radius of the probe beam), $w_{jl} = 2U_0^2 L_{\rm diff} W_{jl}$ ($jl = \{11, 22, 12, 21\}$) are the dimensionless local nonlinear coefficients, $\Re_{jl}(\vec{\zeta}' - \vec{\zeta}) = 2L_{\rm diff} R_0^2 U_0^2 \mathcal{N}'_{jl}[(\vec{\zeta}' - \vec{\zeta})R_0]$, $\tilde{\nabla}_\perp^2 = \partial^2/\partial\xi^2 + \partial^2\partial\eta^2$, $\vec{\zeta} = (\xi, \eta) = (x, y)/R_0$, and $d^2\zeta' = d\xi' d\eta'$.

APPENDIX C: A SHORT DESCRIPTION OF NUMERICS DETAILS

In this Appendix, we give a simple description on the imaginary-time propagation method [49] for numerically finding the steady-state solutions (including stationary optical patterns, solitons, and vortices) of the dimensionless nonlinear Schrödinger equation (7) used in the main text. The basic ideas are the following: (i) Replacing s by $-is$ in the equation, and (ii) normalizing the solution after each step of integration, i.e., $v(\xi, \eta, s + \Delta s) = \frac{v(\xi,\eta,s+\Delta s)}{\|v(\xi,\eta,s+\Delta s)\|}$ to keep the power of the solution to a fixed value.

Based on these ideas, first we replace $s \to -is$ in Eq. (7), which results in the new equation

$$\frac{\partial v_j}{\partial s} = \tilde{\nabla}_\perp^2 v_j + \sum_{l=1,2} \int d^2\zeta' [I_l \Re_{jl}(\vec{\zeta}' - \vec{\zeta})|v_l(\vec{\zeta}', s)|^2] v_j(\vec{\zeta}, s). \tag{C1}$$

Secondly, we solve the above equation (C1) by a split-step Fourier method. The first step is to integrate the diffraction term in momentum space by a fast Fourier transform, and then go back to the spatial coordinate by an inverse Fourier transform; the second step is to carry out the integration on the terms with nonlocal interactions, which is solved by a numerical convolution. Thus we have

$$\frac{d\tilde{v}_j}{ds} = -\beta^2 \tilde{v}_j, \tag{C2a}$$

$$\frac{dv_j}{ds} = \sum_{l=1,2} I_l \mathcal{F}^{-1}\{\mathcal{F}[\Re_{jl}(\vec{\zeta})]\mathcal{F}[|v_l(\vec{\zeta}, s)|^2]\} v_j(\vec{\zeta}, s), \tag{C2b}$$

where $-\beta^2$ and $\tilde{v}_j$ are, respectively, the Fourier transforms of $\tilde{\nabla}_\perp^2$ and v_j; $\mathcal{F}$ and $\mathcal{F}^{-1}$ are, respectively, the symbols of the Fourier transform and the inverse Fourier transform.

The imaginary-time propagation is made in a square domain until the convergence of the intensity distribution $|v_j|^2$ within the error less than 10^{-6}. In the simulation, the initial condition is a plane wave perturbed by Gaussian noise; the boundary condition is a periodic one. The simulations are implemented by using different numerical grids (i.e., 256, 512, and 1024) in the transverse (i.e., ξ and η) directions, which can ensure that the results (including the ones for the MI with short wavelengths) for the different grids will be in agreement with each other.

APPENDIX D: DETAILS FOR THE ALTERNATIVE EMERGENCE OF THE CIRCULAR AND ELLIPTICAL SPOTS IN FIG. 4(a)

Here we give a detailed illustration of the alternative emergence of circular and elliptical spots shown in Fig. 4(a). This steady-state pattern is obtained by numerically solving Eq. (7) by using imaginary propagation together with split-step Fourier methods, by taking the system parameters $(\alpha_{12}/\alpha_{11}, \alpha_{11}) = (0.03, 245)$, $\sigma = 1$, and $\rho_{22}^{(0)}/\rho_{11}^{(0)} = 1$.

Shown in panels (a), (b), and (c) of Fig. 9 are results of dimensionless and normalized probe-field intensities $|v_1|^2$, $|v_2|^2$, and $|v|^2 = |v_1|^2 + |v_2|^2$ as functions of the dimensionless coordinates $\xi = x/R_0$ and $\eta = y/R_0$, respectively. We see that both of the light intensities $|v_1|^2$ and $|v_2|^2$ of the two probe-field components form hexagonal lattices, given, respectively, by Figs. 9(a) and 9(b). However, their superposition, $|v_1|^2 + |v_2|^2$, gives a lattice pattern in which the v_1-component appears to be composed of circular spots but the v_2-component appears to be composed of elliptical spots [see Fig. 9(c)]. The reason for the appearance of such an interesting pattern is that the v_1-component has a hexagonal structure composed of circular bright spots (where light intensity is maximal) in a dark background, while the v_2-component has a hexagonal structure composed of circular dark spots (where light intensity is minimal) in a bright background. As a result, the intensity superposition of the two polarized components (i.e., $|v_1|^2 + |v_2|^2$) gives a pattern in which the circular and elliptical spots appear alternatively. A similar phenomenon also occurs in Fig. 5(a), with the physical reason the same as given above.

APPENDIX E: DERIVATION OF THE CRITERION FOR THE OPTICAL PHASE SEPARATION

We follow the method used in Refs. [53,56,60] to find the criterion for the transition between miscible and immiscible states through minimizing the energy of the system. For the miscible state, the distribution of $v_j = v_j(\vec{\zeta}, s)$ is in the whole space. Using Eq. (12), we have

$$E_{\rm mis} = \sum_{j=1}^{2} \int |\tilde{\nabla}_\perp v_j|^2 d^2\zeta + \frac{1}{2}\sum_{j,l=1}^{2} E_{jl}, \tag{E1}$$

where $E_{jl} = \iint \Re_{jl}(\vec{\zeta}' - \vec{\zeta})|v_j(\vec{\zeta}, s)|^2 |v_l(\vec{\zeta}', s)|^2 d^2\zeta d^2\zeta'$. For simplicity, we consider a homogeneous solution of Eqs. (7). The corresponding energy reads

$$E_{\rm mis} = \frac{1}{2V_{\rm tot}} \int \{I_1^2 \Re_{11}(\vec{\zeta}) + I_2^2 \Re_{22}(\vec{\zeta}) + I_1 I_2 [\Re_{12}(\vec{\zeta}) + \Re_{21}(\vec{\zeta})]\} d^2\zeta, \tag{E2}$$

where $V_{\rm tot} = d^2\zeta$ is the volume of the whole space. For the immiscible state, the two components occupy different positions in space. Assuming V_1 (V_2) is the volume occupied by component 1 (component 2), the overlap integrals in Eq. (E2) will be zero. So the energy of the immiscible state is given by

$$E_{\rm immis} = \sum_{j=1}^{2} \int |\tilde{\nabla}_\perp v_j|^2 d^2\zeta + \frac{1}{2}\sum_{j=1}^{2} E_j, \tag{E3}$$

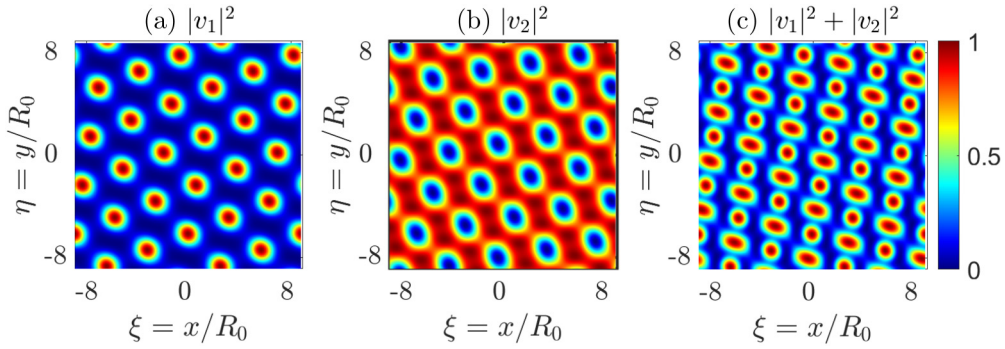

FIG. 9. Optical patterns of the two-component probe field as functions of $\xi = x/R_0$ and $\eta = y/R_0$, by taking $(\alpha_{12}/\alpha_{11}, \alpha_{11}) = (0.03, 245)$, $\sigma = 1$, and $\rho_{22}^{(0)}/\rho_{11}^{(0)} = 1$. (a) The result for $|v_1|^2$, which is a hexagonal lattice with circular bright spots in a dark background. (b) The result for $|v_2|^2$, which is also a hexagonal lattice but with circular bright spots in a bright background. (c) The result for $|v|^2 = |v_1|^2 + |v_2|^2$, which is a linear superposition of the two polarized components, giving a pattern where the circular and elliptical spots appear alternatively.

where $E_j = \iint \Re_{jj}(\vec{\zeta}' - \vec{\zeta})|v_j(\vec{\zeta}, s)|^2|v_j(\vec{\zeta}', s)|^2 d^2\zeta d^2\zeta'$. The integral for $\Re_{jj}$ is for the component j which occupies the volume V_j, with V_1 and V_2 satisfying $V_{\rm tot} = V_1 + V_2$. We obtain

$$E_{\rm immis} = \frac{1}{2V_{\rm tot}}\Bigg[\int \{I_1^2\Re_{11}(\vec{\xi}) + I_2^2\Re_{22}(\vec{\xi})\}d^2\zeta + I_1I_2\bigg(\int \Re_{11}(\vec{\xi})d^2\zeta \times \int \Re_{22}(\vec{\xi})d^2\zeta\bigg)^{1/2}\Bigg]. \tag{E4}$$

The energy difference between the miscible and immiscible state is

$$\Delta E = \frac{I_1I_2}{V_{\rm tot}}\Bigg[\int \frac{1}{2}[\Re_{12}(\vec{\xi}) + \Re_{21}(\vec{\xi})]d^2\zeta - \bigg(\int \Re_{11}(\vec{\xi})d^2\zeta \times \int \Re_{22}(\vec{\xi})d^2\zeta\bigg)^{1/2}\Bigg]. \tag{E5}$$

Therefore, $\Delta E = 0$ defines the critical value (boundary) for the transition from miscible to immiscible systems.

[1] M. Saffman, T. G. Walker, and K. Mølmer, Quantum information with Rydberg atoms, Rev. Mod. Phys. **82**, 2313 (2010).

[2] C. S. Adams, J. D. Pritchard, and J. P. Shaffer, Rydberg atom quantum technologies, J. Phys. B **53**, 012002 (2020).

[3] A. K. Mohapatra, T. R. Jackson, and C. S. Adams, Coherent Optical Detection of Highly Excited Rydberg States Using Electromagnetically Induced Transparency, Phys. Rev. Lett. **98**, 113003 (2007).

[4] J. D. Pritchard, D. Maxwell, A. Gauguet, K. J. Weatherill, M. P. A. Jones, and C. S. Adams, Cooperative Atom-Light Interaction in a Blockaded Rydberg Ensemble, Phys. Rev. Lett. **105**, 193603 (2010).

[5] M. Fleischhauer, A. Imamoğlu, and J. P. Marangos, Electromagnetically induced transparency: Optics in coherent media, Rev. Mod. Phys. **77**, 633 (2005).

[6] O. Firstenberg, C. S. Adams, and S. Hofferberth, Nonlinear quantum optics mediated by Rydberg interactions, J. Phys. B **49**, 152003 (2016).

[7] C. Murray and T. Pohl, Quantum and nonlinear optics in strongly interacting atomic ensembles, in *Advances in Atomic, Molecular, and Optical Physics* (Academic, New York, 2016), Vol. 65, Chap. 7, pp. 321–372.

[8] S. Sevincli, N. Henkel, C. Ates, and T. Pohl, Nonlocal Nonlinear Optics in Cold Rydberg Gases, Phys. Rev. Lett. **107**, 153001 (2011).

[9] J. Stanojevic, V. Parigi, E. Bimbard, A. Ourjoumtsev, and P. Grangier, Dispersive optical nonlinearities in a Rydberg electromagnetically-induced-transparency medium, Phys. Rev. A **88**, 053845 (2013).

[10] A. Grankin, E. Brion, E. Bimbard, R. Boddeda, I. Usmani, A. Ourjoumtsev, and P. Grangier, Quantum-optical nonlinearities induced by Rydberg-Rydberg interactions: A perturbative approach, Phys. Rev. A **92**, 043841 (2015).

[11] P. Bienias and H. P. Büchler, Quantum theory of Kerr nonlinearity with Rydberg slow light polaritons, New J. Phys. **18**, 123026 (2016).

[12] Z. Bai and G. Huang, Enhanced third-order and fifth-order Kerr nonlinearities in a cold atomic system via Rydberg-Rydberg interaction, Opt. Express **24**, 4442 (2016).

[13] A. Tebben, C. Hainaut, V. Walther, Y.-C. Zhang, G. Zürn, T. Pohl, and M. Weidemüller, Blockade-induced resonant enhancement of the optical nonlinearity in a Rydberg medium, Phys. Rev. A **100**, 063812 (2019).

[14] Z. Bai, W. Li, and G. Huang, Stable single light bullets and vortices and their active control in cold Rydberg gases, Optica **6**, 309 (2019).

[15] J. Sinclair, D. Angulo, N. Lupu-Gladstein, K. Bonsma-Fisher, and A. M. Steinberg, Observation of a large, resonant, cross-Kerr nonlinearity in a free-space Rydberg medium, Phys. Rev. Research **1**, 033193 (2019).

[16] Z. Shi, W. Li, and G. Huang, Structural phase transitions of optical patterns in atomic gases with microwave controlled Rydberg interactions, Phys. Rev. A **102**, 023519 (2020).

[17] H. Saito, Y. Kawaguchi, and M. Ueda, Ferrofluidity in a Two-Component Dipolar Bose-Einstein Condensate, Phys. Rev. Lett. **102**, 230403 (2009).

[18] N. Henkel, R. Nath, and T. Pohl, Three-Dimensional Roton Excitations and Supersolid Formation in Rydberg-Excited

Bose-Einstein Condensates, Phys. Rev. Lett. **104**, 195302 (2010).

[19] F. Cinti, P. Jain, M. Boninsegni, A. Micheli, P. Zoller, and G. Pupillo, Supersolid Droplet Crystal in a Dipole-Blockaded Gas, Phys. Rev. Lett. **105**, 135301 (2010).

[20] R. Mottl, F. Brennecke, K. Baumann, R. Landig, T. Donner, and T. Esslinger, Roton-type mode softening in a quantum gas with cavity-mediated long-range interactions, Science **336**, 1570 (2012).

[21] N. Henkel, F. Cinti, P. Jain, G. Pupillo, and T. Pohl, Supersolid Vortex Crystals in Rydberg-Dressed Bose-Einstein Condensates, Phys. Rev. Lett. **108**, 265301 (2012).

[22] C.-H. Hsueh, T.-C. Lin, T.-L. Horng, and W. C. Wu, Quantum crystals in a trapped Rydberg-dressed Bose-Einstein condensate, Phys. Rev. A **86**, 013619 (2012).

[23] C.-H. Hsueh, Y.-C. Tsai, K.-S. Wu, M.-S. Chang, and W. C. Wu, Pseudospin orders in the supersolid phases in binary Rydberg-dressed Bose-Einstein condensates, Phys. Rev. A **88**, 043646 (2013).

[24] G. Labeyrie, E. Tesio, P. M. Gomes, G. L. Oppo, W. J. Firth, G. R. M. Robb, A. S. Arnold, R. Kaiser, and T. Ackemann, Optomechanical self-structuring in a cold atomic gas, Nat. Photon. **8**, 321 (2014).

[25] F. Cinti, T. Macré, W. Lechner, G. Pupillo, and T. Pohl, Defect-induced supersolidity with soft-core bosons, Nat. Commun. **5**, 3235 (2014).

[26] A. Camara, R. Kaiser, and G. Labeyrie, Optical pattern formation with a two-level nonlinearity, Phys. Rev. A **92**, 013820 (2015).

[27] Z.-K. Lu, Y. Li, D. S. Petrov, and G. V. Shlyapnikov, Stable Dilute Supersolid of Two-Dimensional Dipolar Bosons, Phys. Rev. Lett. **115**, 075303 (2015).

[28] H. Kadau, M. Schmitt, M. Wenzel, C. Wink, T. Maier, I. Ferrier-barbut, and T. Pfau, Observing the Rosensweig instability of a quantum ferrofluid, Nature (London) **530**, 194 (2016).

[29] F. Wächtler and L. Santos, Quantum filaments in dipolar Bose-Einstein condensates, Phys. Rev. A **93**, 061603(R) (2016).

[30] F. Maucher, T. Pohl, S. Skupin, and W. Krolikowski, Self-Organization of Light in Optical Media with Competing Nonlinearities, Phys. Rev. Lett. **116**, 163902 (2016).

[31] W. J. Firth, I. Krešić, G. Labeyrie, A. Camara, and T. Ackemann, Thick-medium model of transverse pattern formation in optically excited cold two-level atoms with a feedback mirror, Phys. Rev. A **96**, 053806 (2017).

[32] C.-H. Hsueh, W.-C. Wu, and M. Tsubota, Quantum crystallography of rydberg-dressed bose gases on a square lattice, Phys. Rev. A **95**, 013631 (2017).

[33] Y.-C. Zhang, V. Walther, and T. Pohl, Long-Range Interactions and Symmetry Breaking in Quantum Gases through Optical Feedback, Phys. Rev. Lett. **121**, 073604 (2018).

[34] Y. Li, A. Geibler, W. Hofstetter, and W. Li, Supersolidity of lattice bosons immersed in strongly correlated Rydberg dressed atoms, Phys. Rev. A **97**, 023619 (2018).

[35] K.-T. Xi, T. Byrnes, and H. Saito, Fingering instabilities and pattern formation in a two-component dipolar Bose-Einstein condensate, Phys. Rev. A **97**, 023625 (2018).

[36] Y.-C. Zhang, F. Maucher, and T. Pohl, Supersolidity around a Critical Point in Dipolar Bose-Einstein Condensates, Phys. Rev. Lett. **123**, 015301 (2019).

[37] The two-component probe field considered here is in some sense similar to a mixture of binary fluids, where pattern formation was studied intensively [see, e.g., M. C. Cross and P. C. Hohenberg, Pattern formation outside of equilibrium, Rev. Mod. Phys. **65**, 851 (1993)].

[38] We assume all the atoms are initially populate in the states $|1\rangle$ and $|2\rangle$ equally, and hence the average of any atomic operator $\hat{O}$ amounts to $\langle\hat{O}\rangle = \langle G|\hat{O}|G\rangle$, with $|G\rangle = |1_1, 1_2, \ldots, 1_{N/2}, 2_{N/2+1}, 2_{N/2+2}, \ldots, 2_N\rangle$.

[39] D. A. Steck, Rubidium 87 D Line Data, available online at http://steck.us/alkalidata (Version 2.2.1, last revised 21 November 2019).

[40] K. Singer, J. Stanojevic, M. Weidemuller, and R. Cote, Long-range interactions between alkali Rydberg atom pairs correlated to the ns-ns, np-np and nd-nd asymptotes, J. Phys. B **38**, S295 (2005).

[41] Q. Zhang, Z. Bai, and G. Huang, Fast-responding property of electromagnetically induced transparency in Rydberg atoms, Phys. Rev. A **97**, 043821 (2018).

[42] The nonlinearity length of the system is given by $L_{\rm non} \equiv [U_0^2 \int d^2r'_\perp |N_{11}(\mathbf{r}'_\perp)|]^{-1}$. With this definition, one has $\Re_{jl}(\vec{\zeta}' - \vec{\zeta}) = 2(L_{\rm diff}/L_{\rm non})B_0 N'_{jl}[(\vec{\zeta}' - \vec{\zeta})R_0]$, with $B_0 \equiv R_0^2/\int d^2r_\perp |N_{11}(\mathbf{r}_\perp)|$.

[43] In our consideration, $U_0 = 6.28$MHz, $R_0 \approx 7\mu$m, and $L_{\rm diff} \approx L_{\rm non} = 0.2$ mm.

[44] V. E. Zakharov and L. A. Ostrovsky, Modulation instability: The beginning, Physica D **238**, 540 (2009).

[45] G. Biondini and D. Mantzavinos, Universal Nature of the Nonlinear Stage of Modulational Instability, Phys. Rev. Lett. **116**, 043902 (2016).

[46] W. Krolikowski, O. Bang, and J. Wyller, Modulational instability in nonlocal nonlinear Kerr media, Phys. Rev. E **64**, 016612 (2001).

[47] W. Królikowski, O. Bang, N. I. Nikolov, D. Neshev, J. Wyller, J. J. Rasmussen, and D. Edmundson, Modulational instability, solitons and beam propagation in spatially nonlocal nonlinear media, J. Opt. B. **6**, S288 (2004).

[48] Generally, the growth rate is a complex number, i.e., $\lambda = \lambda_r + i\lambda_i$. We find that λ is either a real number ($\lambda = \lambda_r$) or an imaginary one ($\lambda = i\lambda_i$). Thus in the linear level either the perturbation grows exponentially when $\lambda^2 = \lambda_r^2 > 0$, or it decays exponentially when $\lambda^2 = -\lambda_i^2 < 0$.

[49] J. Yang, *Nonlinear Waves in Integrable and Non-integrable Systems* (SIAM, Philadelphia, 2010).

[50] Note that in our model the two orthogonal, circularly polarized components (σ^+ and σ^-) of the probe field couple the atomic transitions $|1\rangle \leftrightarrow |3\rangle$ and $|2\rangle \leftrightarrow |3\rangle$, respectively. Hence the normalized total probe-field intensity is given by $I = |v_1|^2 + |v_2|^2$.

[51] S. C. Glotzer, D. Stauffer, and N. Jan, Monte Carlo Simulations of Phase Separation in Chemically Reactive Binary Mixtures, Phys. Rev. Lett. **72**, 4109 (1994).

[52] E. Timmermans, Phase Separation of Bose-Einstein Condensates, Phys. Rev. Lett. **81**, 5718 (1998).

[53] P. Ao and S. T. Chui, Binary Bose-Einstein condensate mixtures in weakly and strongly segregated phases, Phys. Rev. A **58**, 4836 (1998).

[54] C. M. Pooley, O. Kuksenok, and A. C. Balazs, Convection-driven pattern formation in phase-separating binary fluids, Phys. Rev. E **71**, 030501(R) (2005).

[55] J. Sabbatini, W. H. Zurek, and M. J. Davis, Phase Separation and Pattern Formation in a Binary Bose-Einstein Condensate, Phys. Rev. Lett. **107**, 230402 (2011).

[56] L. Wen, W. M. Liu, Y. Cai, J. M. Zhang, and J. Hu, Controlling phase separation of a two-component Bose-Einstein condensate by confinement, Phys. Rev. A **85**, 043602 (2012).

[57] V. Shevtsova, Y. A. Gaponenko, V. Sechenyh, D. E. Melnikov, T. Lyubimova, and A. Mialdun, Dynamics of a binary mixture subjected to a temperature gradient and oscillatory forcing, J. Fluid Mech. **767**, 290 (2015).

[58] M. E. Cates and E. Tjhung, Theories of binary fluid mixtures: From phase-separation kinetics to active emulsions, J. Fluid Mech. **836**, P1 (2018).

[59] M. Ota, S. Giorgini, and S. Stringari, Magnetic Phase Transition in a Mixture of Two Interacting Superfluid Bose Gases at Finite Temperature, Phys. Rev. Lett. **123**, 075301 (2019).

[60] R. K. Kumar, L. Tomio, and A. Gammal, Spatial separation of rotating binary Bose-Einstein condensates by tuning the dipolar interactions, Phys. Rev. A **99**, 043606 (2019).

[61] I. Carusotto and C. Ciuti, Quantum fluids of light, Rev. Mod. Phys. **85**, 299 (2013).

[62] In particular, if $\Re_{ij}(\vec{\zeta}) = g_{ij}\delta(\vec{\zeta})$, the definition (14) is simplified to $\Delta E = \frac{I_1 I_2}{V_{\rm tot}}[\frac{1}{2}(g_{12}+g_{21}) - \sqrt{g_{11}g_{22}}]$, which has been used to characterize the phase separation in systems with local nonlinearities (i.e., $\sigma = 0$) [53,56,60]. In this case, the critical value for the transition from the miscibility to the immiscibility is given by $\alpha_{12}/\alpha_{11} = 1$.

[63] D. L. Andrews and M. Babiker, *The Angular Momentum of Light* (Cambridge University Press, Cambridge, 2013).

[64] N. Takei, C. Sommer, C. Genes, G. Pupillo, H. Goto, K. Koyasu, H. Chiba, M. Weidemüller, and K. Ohmori, Direct observation of ultrafast many-body electron dynamics in an ultracold Rydberg gas, Nat. Commun. **7**, 13449 (2016).

[65] A. J. Scroggie, W. J. Firth, G. S. McDonald, M. Tlidi, R. Lefever, and L. A. Lugiato, Pattern formation in a passive kerr cavity, Chaos Solitons Fractals **4**, 1323 (1994).

[66] M. Tlidi, P. Mandel, and M. Haelterman, Spatiotemporal patterns and localized structures in nonlinear optics, Phys. Rev. E **56**, 6524 (1997).

[67] M. Tlidi, A. G. Vladimirov, and P. Mandel, Interaction and stability of periodic and localized structures in optical bistable systems, IEEE J. Quantum Electron. **39**, 216 (2003).

[68] Y. Mu, L. Qin, Z. Shi, and G. Huang, Giant Kerr nonlinearities and magneto-optical rotations in a Rydberg-atom gas via double electromagnetically induced transparency, Phys. Rev. A **103**, 043709 (2021).